DE GRUYTER Open Physics 2025; 23: 20250142

Research Article

Anil Ahlawat, Mukesh Kumar Sharma*, Kaouther Ghachem, Badr M. Alshammari, and Lioua Kolsi*

Impacts of sinusoidal heat flux and embraced heated rectangular cavity on natural convection within a square enclosure partially filled with porous medium and Casson-hybrid nanofluid

https://doi.org/10.1515/phys-2025-0142
received September 14, 2024; accepted March 18, 2025

Abstract: In the current research, the influence of a sinusoidal heat flux and a heated rectangular cavity in a partially porous Casson hybrid nanofluid-filled square enclosure being affected by a constant magnetic field imposed in the *x*-direction having magnitude B_0, on natural convection were investigated numerically. A rectangular heated cavity having width $H/5$ and height $H/2$ was positioned in the middle of the square enclosure. The sinusoidal heat flux of length $H/2$ is positioned centrally at the enclosure's bottom wall, although the top wall is at a lower temperature, say $T_{c,}$ and the rest of the enclosure was insulated. The finite-difference method, combined with the successive over relaxation, successive under relaxation, and Gauss–Siedel techniques, is employed to address the challenge of solving the nonlinear coupled governing partial differential equations of motion and energy. Numerical calculations were carried out using the values of the relevant parameters in the range $0 \leq \text{Ha} \leq 15$, $10^4 \leq \text{Ra} \leq 10^6$, $0.00 \leq \phi_{\text{hnf}} \leq 0.04$, $10^{-5} \leq \text{Da} \leq 10^{-3}$, $0.1 \leq \gamma \leq 1$, $4 \leq N \leq 12$. The Kirpichev heat number ($K_i = 1$) and Prandtl number ($\text{Pr} = 6.26$) are fixed throughout the study. Contour plots for isotherms and streamlines were plotted to ascertain the impacts of distinct factors on them. The results of this investigation suggest that the heat transfer rate rises as ϕ_{hnf}, Ra, and γ rise and reduce as the Ha and N rises. Finally, it has been observed that decreasing the heated rectangular cavity's aspect ratio leads to a substantial enhancement in heat transfer from both the heat flux and the heated rectangular cavity.

Keywords: natural convection, Casson fluid, hybrid nanofluid, heated rectangular cavity, average Nusselt number

Nomenclature

B_0	magnetic field intensity (T)
C_p	specific heat per unit mass (J kg^{-1} K^{-1})
$\text{Nu}_{\text{Local}^{\text{hb}}}$	local Nusselt number at inner heated rectangular cavity
$\text{Nu}_{\text{Local}^{\text{hf}}}$	local Nusselt number at heat flux
$\text{Nu}_{\text{avg}^{\text{hb}}}$	average Nusselt number at inner heated rectangular cavity
$\text{Nu}_{\text{avg}^{\text{hf}}}$	average Nusselt number at heat flux
Da	Darcy number
$\vec{g}$	gravitational acceleration (m s^{-2})
H	length and width of square cavity (m)
Ha	Hartmann number
k	thermal conductivity (Wm^{-1} K^{-1})
K	permeability of porous medium
K_i	Kirpichev heat number
N	periodicity parameter
P	dimensionless pressure
p	pressure (Pa)
Pr	Prandtl number
$\vec{q}$	velocity vector
Ra	Rayleigh number

*** Corresponding author: Mukesh Kumar Sharma,** Department of Mathematics, Guru Jambheshwar University of Science and Technology, Hisar, 125001, India, e-mail: drms123@gmail.com

*** Corresponding author: Lioua Kolsi,** Department of Mechanical Engineering, College of Engineering, University of Ha'il, Ha'il, 81451, Saudi Arabia, e-mail: lioua_enim@yahoo.fr

Anil Ahlawat: Department of Mathematics and Statistics, Manipal University Jaipur, Jaipur, Rajasthan, 303007, India; Department of Mathematics, Guru Jambheshwar University of Science and Technology, Hisar, 125001, India, e-mail: anilahlawat409@gmail.com

Kaouther Ghachem: Department of Industrial and Systems Engineering, College of Engineering, Princess Nourah bint Abdulrahman University, P.O.Box 84428, Riyadh, 11671, Saudi Arabia, e-mail: kgmaatki@pnu.edu.sa

Badr M. Alshammari: Department of Electrical Engineering, College of Engineering, University of Ha'il, Ha'il, 81451, Saudi Arabia, e-mail: bms.alshammari@uoh.edu.sa

T	dimensional temperature (K)
u, U	dimensional and dimensionless velocity along the x-axis (m s^{-1})
v, V	dimensional and dimensionless velocity along the y-axis (m s^{-1})
X, Y	dimensionless Cartesian co-ordinates
x, y	dimensional Cartesian co-ordinates (m)
ε	porosity

Greek symbols

α	thermal diffusivity (m^2 s^{-1})
β	volumetric thermal expansion coefficient (K^{-1})
γ	Casson fluid parameter
μ	dynamic viscosity (k gm^{-1} s^{-1})
ν	kinematic viscosity (m^{-2} s^{-1})
ρ	density (k gm^{-3})
ϕ	volume concentration of nanoparticles
ω	dimensionless vorticity function
ψ	dimensionless stream function
θ	dimensionless temperature

Subscripts

Al_2O_3	aluminium oxide
Cu	copper
eff	effective
f	base fluid
hnf	hybrid nanofluid
p	porous medium

Abbreviations

AR	aspect ratio
FDM	finite difference method
HTFs	heat transfer fluids
PDEs	partial differential equations
SOR	successive over relaxation
SUR	successive under relaxation

1 Introduction

Convective heat transfer through enclosures (open or closed) is gaining significant interest in light of its numerous real-world applications, which range from everyday used thermal equipment to the cooling of buildings and electrical components. Heat storage capabilities of a thermal system affect its thermal performance. In thermal systems, heat-transfer fluids (HTFs) are being utilized for heat transportation. The design of the thermal system, the stability of the fluid, and its existence are all major factors in selecting HTFs. Conventional HTFs, such as water, air, vapor, natural oils, *etc.*, have been used for a long time, but the poor thermal conductivity of these conventional HTFs limits them to low heat convection. Choi and Eastman [1] invented an alternate known as “nanofluids” to strengthen the thermal conductivity of these HTFs by incorporating nanoparticles of metal and metal oxides (size of particles less than or equal to 100 nm) into a base fluid. In recent decades, a significant number of studies [2–8] on the preparation and implementations of nanofluids has been documented in the published literature. In modification of the “thermal conductivity” of convectional HTFs beyond the single material type nanofluid, the hybrid nanofluids are synthesized. The augmentation in thermal conductivity of fluid utilizing hybrid nanoparticles was initially examined by Jana *et al.* [9] experimentally.

Heat transfer and flow properties of a nanofluid contained in an oblique square cavity were examined by Al Kalbani *et al.* [10] who observed that with increasing Ra and volume percentage of nanoparticles, the heat transmission rate rises and also found that the heat transfer process with blade-shaped nanoparticle is faster than any other shapes. Mansour *et al.* [11] and Rashad *et al.* [12] explored the effects of the size and positioning of a heat sink and source on natural convection within a porous enclosure filled with different types of nanofluids. Furthermore, Armaghani *et al.* [13] explored the intriguing effects of discrete heat source placement on heat transfer and entropy generation within an open inclined L-shaped cavity filled with Ag–water nanofluid. Influence of a stationary magnetic field on the enhancement of heat convection in a rectangular enclosure having diagonal vents, filled with copper–water nanofluid, four individual heaters mounted in the middle of the enclosure walls, and embedded with square-shaped heated block numerically examined by Ushachew *et al.* [14]. They noted that heat convection escalates on the surging concentration of nanoparticles, whereas attenuated with the rise in magnetic field strength. Nishad *et al.* [15] determined the heat convection and flow characteristics of Cu–water nanofluid flowing through a wavy enclosure and observed improvement in heat convection with increasing nanoparticles’ proportion and Rayleigh number, whereas declined with the rise in Hartmann number. The primary cause of the rise in system’s temperature is the waste of energy supplied to the system during the heat transfer process. The optimal and efficient utilization of renewable energy has constantly been the primary objective throughout both industrial and academic communities. Porous media are often used to boost heat convection. Nanofluid flow in cavities that are filled with porous materials, either partially or entirely, has been the primary objective of studies conducted by Sun and Pop [16], Chamkha and Ismael [17], and Sheremet *et al.* [18]. The characteristics of nanofluid flow and the transfer of heat in a foam-filled cylinder under radial injection were investigated by Sharma *et al.* [19]. Vedavathi *et al.* [20] and Venkatadri *et al.* [21] studied the natural convection phenomenon in a semi-trapezoidal/right-angle trapezoidal porous cavity employing "Darcy–Boussinesq approximation and Tiwari and Das' nanofluid model." Venkatadri *et al.* [22] investigated hydromagnetic laminar natural convection in a quadrant-shaped enclosure with an electrically conductive liquid under radiative effects utilizing finite difference methodology and revealed that the Nusselt number increases with higher Rayleigh number and radiative parameter, while it significantly decreases with a greater Hartmann number.

Rheological characteristics of non-Newtonian fluids are positively influencing their utilization in engineering, industry, biology, and other fields of science. The study of non-Newtonian fluids is problematic for researchers due to the nonlinear character of equations. There are various noteworthy non-Newtonian fluid models, but one in particular "Casson fluid model" introduced by Casson [23] is defined as "the liquid which is supposed to have an infinite viscosity at zero rate of shear and zero viscosity at infinite rate of shear." Honey, tomato sauce, jelly, melted chocolates, *etc.,* are different types of real liquids that can be accurately described by the Casson fluid model. Pop and Sheremet [24] performed a computational analysis to examine the phenomenon of natural convection within a square enclosure exposed to differential heating and filled using Casson fluid while considering the impacts of "thermal radiation and viscous dissipation" and observed that the Casson parameter increases heat convection whereas, with a rise in Eckert number, heat transport is reduced.

Hamid *et al.* [25] discussed the heat convection and flow simulations of Casson fluid contained in a trapezoidal cavity, subjected to partial heating from the bottom side and determined that the velocity of the flowing fluid declines and heat convection enhances as the Casson fluid parameter increases. Aghighi *et al.* [26] employed Casson fluid to examine the process of free convection within a square cavity. Aneja *et al.* [27] employed a porous square enclosure containing Casson fluid to perform numerical investigations on natural convection processes. Devi *et al.* [28] carried out a computational study to analyze the properties of natural convection and flow of fluid in a square cavity filled with Casson fluid. Sivasankaran *et al.* [29] performed simulations numerically in order to learn how thermal radiation and porous region affects the process of heat convection and flow pattern in a Casson fluid-filled square cavity. The Brinkman model was utilized by Yasmin *et al.* [30] to describe the thermal and flow properties of a magnetohydrodynamic Casson nanofluid inside a non-uniformly heated square cavity. Munir and Turabi [31] examined the effects of a non-planar heated bottom wall, hybrid nanofluid, and inclined magnetic field on the natural convection within a triangular cavity having a cooled cylinder and revealed that heat transfer rate enhanced with an increase in undulations of non-planar wall and higher wave amplitude but diminishes with an increase in magnetic field strength. In recent studies, Hussain *et al.* [32], Ganesh *et al.* [33], and Turabi and Munir [34] employed the Casson fluid model to understand heat convection in different enclosures.

Not enough is being done in this research area to meet the standards of current engineering and technology requirements. In light of the reviewed literature, the present study is inspired to extend the applications of Casson fluid in natural convection by employing a hybrid nanofluid. To the extent of our best understanding, an investigation of this kind has never been carried out in the past. So, this study aims to fill that gap by examining the dual heating mechanism, featuring both sinusoidal heat flux and an embraced heated rectangular cavity, which profoundly impacts the natural convection process. A key highlight of this work is its investigation into the interaction between partially porous media and fluid flow, shedding light on the intricate thermal and hydrodynamic behaviors within porous structures. This configuration, with its ability to introduce thermal resistance and dampen flow, significantly influences convection patterns. These findings hold critical implications for the design optimization of advanced energy storage systems and heat exchangers. The proposed model serves as a conceptual framework for simulating heat exchange systems in automobiles, where filters act as porous media, a heated shaft is immersed in lubricant, and heat flux arises from the surroundings. Also, these innovative aspects are pivotal for advancing thermal management systems across various engineering applications, such as cooling technologies and environmental engineering, by optimizing heat transfer processes in intricate fluid and geometric configurations. Therefore, this work helps to ensure efficient and sustainable thermal solutions. The primary concerns motivating this current research are delineated as follows:

- How do variations in the porosity of the medium and the hybrid nanofluid composition impact the convective heat transfer coefficient and flow dynamics?
- How does Casson fluid dynamics influence the efficiency of heat transfer?
- What role does the heated rectangular cavity play in enhancing or modifying the heat transfer characteristics within the enclosure?
- What are the effects of sinusoidal heat flux on the natural convection and heat transfer performance within a square enclosure partially filled with a porous medium and Casson-hybrid nanofluid?

2 Mathematical model

A graphical outline of the current study under investigation is depicted in Figure 1, along with the associated grid generation process. The side length of the square enclosure is H. A layer with a porous structure having H width and $H/2$ height is located adjacent to the lower wall of the enclosure. A rectangular cavity of sides $H/2$ and $H/5$ heated at temperature T_h is positioned in the center, inside the enclosure. A sinusoidal heat flux of $H/2$ length is positioned in the center of the lower wall, and the top wall is kept at the temperature T_c ($T_c < T_h$), whereas adjacent vertical walls are insulated. The porous stratum at the fluid interface is supposed to be permeable, allowing crossflow from fluid-to-porous medium. The Casson fluid model was integrated into this study to represent the non-Newtonian characteristics of the working fluid. Casson fluids exhibit a shear-thinning behavior with a defined yield stress. This model is particularly relevant for engineering and industrial applications involving complex fluids such as lubricants, biological fluids, and polymer solutions. By combining the Casson fluid model with the hybrid nanofluid, the study provides a framework to explore advanced thermal fluids that not only enhance thermal conductivity through nanoparticles (Cu and Al_2O_3) but also adapt to varying shear conditions for improved flow and heat transfer control. The current mathematical model for natural convective systems is formulated under the following assumptions:

- The base fluid (H_2O) and nanoparticles (Cu and Al_2O_3) are in the state of thermal stability.
- The enclosure occupies single-phase H_2O-based Casson hybrid nanofluid, and the lower half region of the enclosure is filled with a porous medium that is saturated with the same hybrid nanofluid.
- The flow is laminar, two-dimensional, steady, and incompressible.
- The density variation is modeled using the Boussinesq approximation, while the remaining thermophysical properties are assumed constant and provided in Table 1.
- The influences of viscous dissipation and Joule heating are considered negligible throughout this study.

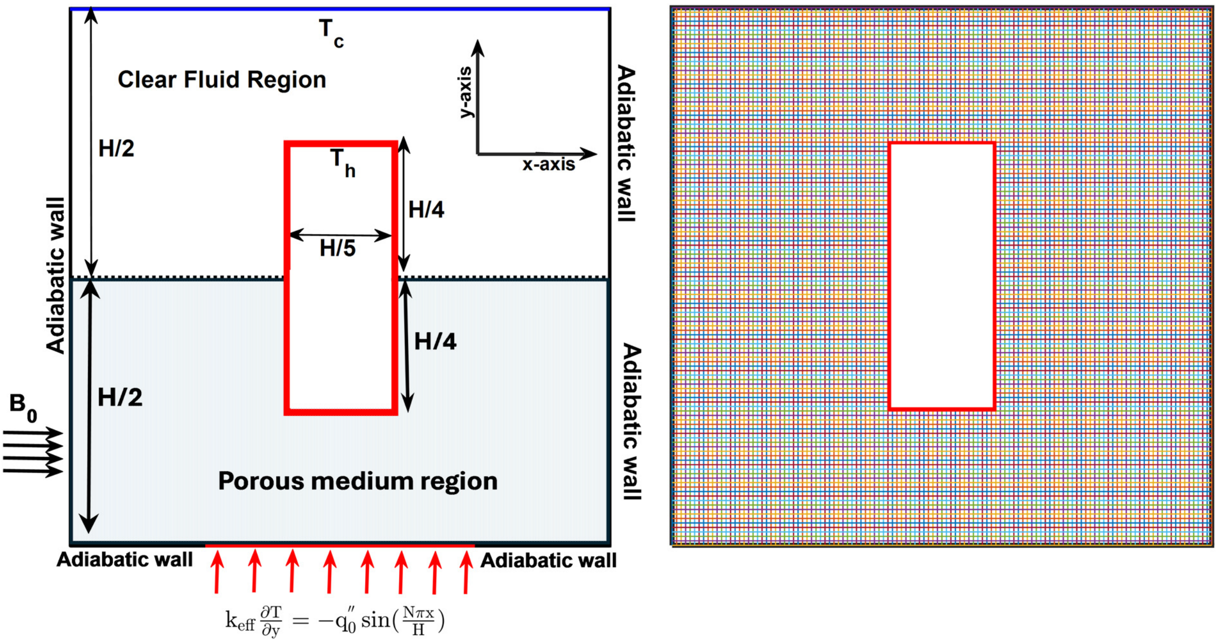

(a) (b)

Figure 1: Representation of physical domain (a) and view of its grid's discretization 121 × 121 (b).

Table 1: Thermo-physical properties of nanoparticles (Al_2O_3 and Cu) and base fluid (H_2O) [35,36]

Property	H_2O	Cu	Al_2O_3
ρ (kg m^{-3})	997.1	8,933	3,970
c_p (J kg^{-1} K^{-1})	4,179	385	765
k (W m^{-1} K^{-1})	0.613	401	40
β (K^{-1})	21×10^{-5}	1.67×10^{-5}	0.85×10^{-5}

- The enclosure is divided into two equal-sized regions, with the lower region fully occupied by a Darcian, incompressible, homogeneous, and isotropic porous medium.
- The solid boundaries are assumed to satisfy the no-slip condition.
- The influences of Brownian motion and thermophoresis are deemed insignificant.
- A static magnetic field of strength B_0 is aligned horizontally.

The thermophysical properties of the Casson-hybrid nanofluid were derived by incorporating empirical and theoretical formulations. The viscosity of the fluid was modeled to reflect its dependence on the shear rate, as governed by the Casson model, while the effective thermal conductivity was calculated using established hybrid nanofluid models. This integration allows for a comprehensive examination of the interaction between non-Newtonian behavior, enhanced thermal conductivity, and natural convection within the partially porous enclosure. The constitutive equation for an isotropic and incompressible Casson fluid flow is given as follows [28]:

$$\tau_{ij} = \begin{cases} 2\left(\mu_B + \dfrac{p_y}{\sqrt{2\pi}}\right)e_{ij}, & \pi > \pi_c, \\ 2\left(\mu_B + \dfrac{p_y}{\sqrt{2\pi_c}}\right)e_{ij}, & \pi < \pi_c. \end{cases} \tag{2.1}$$

Here, $\pi = e_{ij}e_{ij}$ and e_{ij} are the (i, j)th components of the rate of strain tensor, π_c is the critical value that depends on the type of non-Newtonian model, μ_B is the dynamic viscosity of Casson fluid, and p_y is the yield stress.

2.1 Governing equations

The equations that govern the flow in their dimensionless form, incorporating aforementioned assumptions and the dimensionless parameters from Aneja *et al.* [27] and defined in Eq. (2.2), are written together for the porous and fluidic regions in Eqs. (2.3)–(2.6) in accordance with Sivasankaran *et al.* [29]:

$$\begin{aligned} X &= \frac{x}{H}, \quad Y = \frac{y}{H}, \quad U_{p,hnf} = \frac{u_{p,hnf}H}{\alpha_f}, \quad V_{p,hnf} \\ &= \frac{v_{p,hnf}\mathrm{H}}{\alpha_f}, \quad \theta_{hnf} = \frac{T_{hnf} - T_c}{T_h - T_c},\ \theta_p = \frac{T_p - T_c}{T_h - T_c}, \mathrm{Pr} \\ &= \frac{\nu_f}{\alpha_f}, \mathrm{Da} = \frac{K}{H^2}, \mathrm{Ra} = \frac{g\beta_f(T_h - T_c)H^3}{\nu_f\alpha_f}, \mathrm{P} \\ &= \frac{pH^2}{\rho_f \quad \alpha_f^2}, \mathrm{Ha} = B_0H\sqrt{\frac{\sigma_f}{\mu_f}}, \gamma = \mu_B\frac{\sqrt{2\pi_c}}{\frac{\partial \mathrm{p}}{\partial \mathrm{y}}}, \end{aligned} \tag{2.2}$$

where Pr, Da, K, Ha, γ, and Ra are Prandtl number, Darcy number, permeability of porous medium, Hartmann number, Casson fluid parameter, and Rayleigh number, respectively, and the subscripts "f" used for fluid, "p" for porous, and "hnf" for hybrid nanofluid, and $\vec{q}_{p,hnf} = (U_{p,hnf}, V_{p,hnf})$ is the velocity vector. The Rayleigh number (Ra) highlights the competition between buoyancy and thermal diffusion, influencing convection intensity. The Hartmann number (Ha) captures magnetic field effects, where higher values suppress flow through Lorentz forces. The Darcy number (Da) signifies porous medium permeability, affecting fluid flow and heat transfer. The Casson fluid parameter (γ) reflects the non-Newtonian shear-thinning behavior, which is critical for advanced fluids. The Prandtl number (Pr) links momentum and thermal diffusivity, while nanoparticle volume fraction (ϕ_{hnf}) quantifies enhancements in thermal conductivity.

Continuity equation

$$\nabla\cdot\vec{q}_{p,hnf} = 0. \tag{2.3}$$

Momentum equations

$$\begin{aligned} (\vec{q}_{p,hnf}\cdot\nabla)U_{p,hnf} = {} & -\varepsilon^2\left(\frac{\rho_f}{\rho_{hnf}}\right)\frac{\partial P}{\partial X} + \varepsilon\mathrm{Pr}\left(\frac{\mu_{hnf}}{\mu_f}\right)\left(\frac{\rho_f}{\rho_{hnf}}\right)\left(1\right. \\ & \left. + \frac{1}{\gamma}\right)\left[\frac{\partial^2}{\partial X^2}(U_{p,hnf}) + \frac{\partial^2}{\partial Y^2}(U_{p,hnf})\right] \\ & - \delta\left(\frac{\mu_{hnf}}{\mu_f}\right)\left(\frac{\rho_f}{\rho_{hnf}}\right)\varepsilon^2\frac{\mathrm{Pr}}{\mathrm{Da}}U_{p,hnf}, \end{aligned} \tag{2.4}$$

$$\begin{aligned} (\vec{q}_{p,hnf}\cdot\nabla)V_{p,hnf} = {} & -\varepsilon^2\left(\frac{\rho_f}{\rho_{hnf}}\right)\frac{\partial \mathrm{P}}{\partial \mathrm{Y}} + \varepsilon\mathrm{Pr}\left(\frac{\mu_{hnf}}{\mu_f}\right)\left(\frac{\rho_f}{\rho_{hnf}}\right)\left(1\right. \\ & \left. + \frac{1}{\gamma}\right)\left[\frac{\partial^2}{\partial X^2}(V_{p,hnf}) + \frac{\partial^2}{\partial Y^2}(V_{p,hnf})\right] \\ & - \delta\left(\frac{\mu_{hnf}}{\mu_f}\right)\left(\frac{\rho_f}{\rho_{hnf}}\right)\varepsilon^2\frac{\mathrm{Pr}}{\mathrm{Da}}V_{p,hnf} \\ & + \frac{(\rho\beta)_{hnf}}{\rho_{hnf}\beta_f}\varepsilon^2\,\mathrm{PrRa}\theta_{p,hnf} \\ & - \left(\frac{\rho_f}{\rho_{hnf}}\right)\left(\frac{\sigma_{hnf}}{\sigma_f}\right)\varepsilon^2\mathrm{Ha}^2\mathrm{Pr}V_{p,hnf}. \end{aligned} \tag{2.5}$$

Energy equation

$$(\vec{q}_{\mathrm{p,hnf}}\cdot\nabla)\theta_{\mathrm{p,hnf}} = \left(\frac{\alpha^*}{\alpha_{\mathrm{f}}}\right)\left[\frac{\partial^2}{\partial X^2}(\theta_{\mathrm{p,hnf}}) + \frac{\partial^2}{\partial Y^2}(\theta_{\mathrm{p,hnf}})\right], \tag{2.6}$$

where $\nabla = \frac{\partial}{\partial X}\hat{i} + \frac{\partial}{\partial Y}\hat{j}$ is the gradient operator. The region of hybrid nanofluid and the region of fluid-saturated porous medium are identified as

For clear hybrid nanofluid domain: $\varepsilon = 1$, $\delta = 0$, $\alpha^* = \alpha_{\mathrm{hnf}}$, $\vec{q}_{\mathrm{p,hnf}} = (U_{\mathrm{hnf}}, V_{\mathrm{hnf}})$, $\omega_{\mathrm{p,hnf}} = \omega_{\mathrm{hnf}}$, $\psi_{\mathrm{p,hnf}} = \psi_{\mathrm{hnf}}$ and for fluid-saturated porous regions: $\varepsilon = \varepsilon$, $\delta = 1$, $\alpha^* = \alpha_{\mathrm{eff}}$, $\vec{q}_{\mathrm{p,hnf}} = (U_{\mathrm{p}}, V_{\mathrm{p}})$, $\omega_{\mathrm{p,hnf}} = \omega_{\mathrm{p}}$, $\psi_{\mathrm{p,hnf}} = \psi_{\mathrm{p}}$. The porous medium's porosity (ε) is constant and taken $\varepsilon = 0.398$ throughout the study. Thermophysical properties of the hybrid nanofluid, in relation to nanoparticle volume concentration ($\phi_{\mathrm{Al_2O_3}}$ and ϕ_{cu}), are described as follows [37]:

$$\left.\begin{aligned}
\phi_{\mathrm{hnf}} &= \phi_{\mathrm{Cu}} + \phi_{\mathrm{Al_2O_3}} \\
\rho_{\mathrm{hnf}} &= (1-\phi_{\mathrm{hnf}})\rho_{\mathrm{f}} + \phi_{\mathrm{Cu}}\rho_{\mathrm{Cu}} + \phi_{\mathrm{Al_2O_3}}\rho_{\mathrm{Al_2O_3}} \\
(\rho\beta)_{\mathrm{hnf}} &= (1-\phi_{\mathrm{hnf}})\rho_{\mathrm{f}} + \phi_{\mathrm{Cu}}(\rho\beta)_{\mathrm{Cu}} + \phi_{\mathrm{Al_2O_3}}(\rho\beta)_{\mathrm{Al_2O_3}} \\
(\rho C_{\mathrm{p}})_{\mathrm{hnf}} &= (1-\phi_{\mathrm{hnf}})\rho_{\mathrm{f}} + \phi_{\mathrm{Cu}}(\rho C_{\mathrm{p}})_{\mathrm{Cu}} + \phi_{\mathrm{Al_2O_3}}(\rho C_{\mathrm{p}})_{\mathrm{Al_2O_3}} \\
\alpha_{\mathrm{hnf}} &= \frac{k_{\mathrm{hnf}}}{(\rho C_{\mathrm{p}})_{\mathrm{hnf}}}; \alpha_{\mathrm{eff}} = \frac{k_{\mathrm{eff}}}{(\rho C_{\mathrm{p}})_{\mathrm{hnf}}} \quad \text{where } k_{\mathrm{eff}} \\
&= (1-\varepsilon)k_{\mathrm{s}} + \varepsilon k_{\mathrm{hnf}}
\end{aligned}\right\}. \tag{2.7}$$

where$(\rho C_{\mathrm{p}})_{\mathrm{hnf}}$ is the heat capacity of hybrid nanofluid. In order to provide a description of the expression for the thermal conductivity of hybrid nanofluids (k_{hnf}), the Maxwell [38] model is utilized, and the corresponding expression is given as follows:

$$k_{\mathrm{hnf}} = \left[\frac{\left(\frac{\phi_{\mathrm{Cu}}k_{\mathrm{Cu}} + \phi_{\mathrm{Al_2O_3}}k_{\mathrm{Al_2O_3}}}{\phi_{\mathrm{hnf}}} + 2k_{\mathrm{f}}\right) + 2(\phi_{\mathrm{Cu}}k_{\mathrm{Cu}} + \phi_{\mathrm{Al_2O_3}}k_{\mathrm{Al_2O_3}}) - 2\phi_{\mathrm{hnf}}k_{\mathrm{f}}}{\left(\frac{\phi_{\mathrm{Cu}}k_{\mathrm{Cu}} + \phi_{\mathrm{Al_2O_3}}k_{\mathrm{Al_2O_3}}}{\phi_{\mathrm{hnf}}} + 2k_{\mathrm{f}}\right) - (\phi_{\mathrm{Cu}}k_{\mathrm{Cu}} + \phi_{\mathrm{Al_2O_3}}k_{\mathrm{Al_2O_3}}) + \phi_{\mathrm{hnf}}k_{\mathrm{f}}}\right]k_{\mathrm{f}}. \tag{2.8}$$

The viscosity of hybrid nanofluids (μ_{hnf}) is determined using the following Eq. (2.9), which is based on the Brinkman [39] model

$$\mu_{\mathrm{hnf}} = \frac{\mu_{\mathrm{f}}}{(1-\phi_{\mathrm{hnf}})^{2.5}}. \tag{2.9}$$

The pressure gradient term from the momentum equations is removed with the stream function defined as $U_{\mathrm{p,hnf}} = \frac{\partial}{\partial Y}(\psi_{\mathrm{p,hnf}})$, $V_{\mathrm{p,hnf}} = -\frac{\partial}{\partial X}(\psi_{\mathrm{p,hnf}})$ and $-\omega_{\mathrm{p,hnf}} = \frac{\partial}{\partial Y}(U_{\mathrm{p,hnf}}) - \frac{\partial}{\partial X}(V_{\mathrm{p,hnf}})$, then resultant equations in the form of stream function (ψ) and vorticity (ω) are given in the following equations:

Equation of continuity

$$\nabla^2\psi_{\mathrm{p,hnf}} = -\omega_{\mathrm{p,hnf}}. \tag{2.10}$$

Momentum equation

$$\begin{aligned}
&\frac{\partial}{\partial Y}(\psi_{\mathrm{p,hnf}})\frac{\partial}{\partial X}(\omega_{\mathrm{p,hnf}}) - \frac{\partial}{\partial X}(\psi_{\mathrm{p,hnf}})\frac{\partial}{\partial Y}(\omega_{\mathrm{p,hnf}}) \\
&= \varepsilon\mathrm{Pr}\left(\frac{\mu_{\mathrm{hnf}}}{\mu_{\mathrm{f}}}\right)\left(\frac{\rho_{\mathrm{f}}}{\rho_{\mathrm{hnf}}}\right)\left(1 + \frac{1}{\gamma}\right)\nabla^2\omega_{\mathrm{p,hnf}} \\
&\quad - \left(\frac{\mu_{\mathrm{hnf}}}{\mu_{\mathrm{f}}}\right)\left(\frac{\rho_{\mathrm{f}}}{\rho_{\mathrm{hnf}}}\right)\delta\varepsilon^2\frac{\mathrm{Pr}}{\mathrm{Da}}\omega_{\mathrm{p,hnf}} \\
&\quad + \mathrm{Ha}^2\mathrm{Pr}\varepsilon^2\left(\frac{\sigma_{\mathrm{hnf}}}{\sigma_{\mathrm{f}}}\right)\left(\frac{\rho_{\mathrm{f}}}{\rho_{\mathrm{hnf}}}\right)\left(\frac{\partial^2}{\partial X^2}(\psi_{\mathrm{p,hnf}})\right) \\
&\quad + \frac{(\rho\beta)_{\mathrm{hnf}}}{\rho_{\mathrm{hnf}}\beta_{\mathrm{f}}}\varepsilon^2\,\mathrm{PrRa}\frac{\partial}{\partial X}(\theta_{\mathrm{p,hnf}}).
\end{aligned} \tag{2.11}$$

Energy equation

$$\begin{aligned}
&\frac{\partial}{\partial Y}(\psi_{\mathrm{p,hnf}})\frac{\partial}{\partial X}(\theta_{\mathrm{p,hnf}}) - \frac{\partial}{\partial \mathrm{X}}(\psi_{\mathrm{p,hnf}})\frac{\partial}{\partial \mathrm{Y}}(\theta_{\mathrm{p,hnf}}) \\
&= \frac{\alpha^*}{\alpha_{\mathrm{f}}}(\nabla^2\theta_{\mathrm{p,hnf}}),
\end{aligned} \tag{2.12}$$

where $\nabla^2 = \frac{\partial^2}{\partial X^2} + \frac{\partial^2}{\partial Y^2}$ is the Laplacian operator.

The reduced non-dimensional boundary conditions (BCs) on enclosure's wall are

$$\left.\begin{aligned}
&\psi_{\mathrm{hnf}} = 0, \quad \theta_{\mathrm{hnf}} = 0, \quad \omega_{\mathrm{hnf}} = -\left(\frac{\partial^2\psi_{\mathrm{hnf}}}{\partial Y^2}\right) \quad \text{at} \\
&Y = 1 \text{ and } \psi_{\mathrm{p}} = 0, \quad \omega_{\mathrm{p}} = -\left(\frac{\partial^2\psi_{\mathrm{p}}}{\partial Y^2}\right) \text{at } Y = 0 \\
&\psi_{\mathrm{p,hnf}} = 0, \quad \frac{\partial}{\partial X}(\theta_{\mathrm{p,hnf}}) = 0, \text{ and} \\
&\omega_{\mathrm{p,hnf}} = -\left(\frac{\partial^2}{\partial X^2}(\psi_{\mathrm{p,hnf}})\right) \quad \text{at } X = 0,\ 1 \\
&\frac{\partial\theta_{\mathrm{p}}}{\partial Y} = -K_i\frac{k_{\mathrm{f}}}{k_{\mathrm{eff}}}\sin(N\pi X), \\
&0.25 \le X \le 0.75, \text{ and } Y = 0 \\
&\frac{\partial\theta_{\mathrm{p}}}{\partial Y} = 0, \text{ at } 0 \le X \le 0.25,\ 0.75 < X \le 1, \text{ and } Y = 0.
\end{aligned}\right\} \tag{2.13}$$

The BCs at the sides of the inner heated rectangular cavity are as follows:

$$\left.\begin{aligned}
&\theta_{\mathrm{p,hnf}}(X, Y) = 1, \quad \text{at } Y = 0.25, 0.75 \quad \text{where} \\
&0.4 \le X \le 0.6 \\
&\theta_{\mathrm{p,hnf}}(X, Y) = 1, \quad \text{at } X = 0.4, 0.6 \quad \text{where} \\
&0.25 \le Y \le 0.75.
\end{aligned}\right\} \tag{2.14}$$

Kirpichev heat number ($K_i = q''H/(k_{\mathrm{f}}\Delta T)$) is considered to be equal to one throughout all calculations. The BCs at the interface are obtained by equating "the tangential velocities, normal velocities, shear and normal stresses, temperature, and the heat flux across the interface, and considering same dynamic viscosity ($\mu_{\mathrm{p}} = \mu_{\mathrm{hnf}}$) in both porous and fluid regions, as explained by Chamkha and Ismael [40].” Hence, interface BCs at $Y = 0.5$ reduces to

$$\left.\begin{aligned} &\theta_{\mathrm{hnf}} = \theta_{\mathrm{p}};\ \psi_{\mathrm{hnf}} = \psi_{\mathrm{p}};\quad \omega_{\mathrm{hnf}} = \omega_{\mathrm{p}} \\ &\frac{k_{\mathrm{hnf}}}{k_{\mathrm{eff}}}\frac{\partial\theta_{\mathrm{hnf}}}{\partial Y} = \frac{\partial\theta_{\mathrm{p}}}{\partial Y};\ \frac{\partial\psi_{\mathrm{hnf}}}{\partial Y} = \frac{\partial\psi_{\mathrm{p}}}{\partial Y};\ \frac{\partial\omega_{\mathrm{hnf}}}{\partial Y} = \frac{\partial\omega_{\mathrm{p}}}{\partial Y}. \end{aligned}\right\} \tag{2.15}$$

2.2 Local and average Nusselt number

Local and average Nusselt numbers are estimated together across the heat flux and at the implanted heated rectangular cavity by utilizing the formulas given in the following equations:

Local Nusselt number ($\mathrm{Nu}_{\mathrm{Local}^{\mathrm{hf}}}$) at the heat flux:

$$\mathrm{Nu}_{\mathrm{Local}^{\mathrm{hf}}} = K_i\frac{k_{\mathrm{eff}}}{k_{\mathrm{f}}}\left(\frac{\sin(N\pi X)}{\theta_{\mathrm{p}}}\right). \tag{2.16}$$

Average Nusselt number ($\mathrm{Nu}_{\mathrm{avg}^{\mathrm{hf}}}$) at the heat flux:

$$\mathrm{Nu}_{\mathrm{avg}^{\mathrm{hf}}} = \frac{1}{0.5}\int_{0.25}^{0.75}\mathrm{Nu}_{\mathrm{Local}^{\mathrm{hf}}}\ \mathrm{d}X. \tag{2.17}$$

Local Nusselt number at the portion of inner heated rectangular cavity embraced in the porous layer:

$$\mathrm{Nu}_{\mathrm{Local}^{\mathrm{hb}}} = \frac{k_{\mathrm{eff}}}{k_{\mathrm{f}}}\left(\frac{\partial\theta_{\mathrm{p}}}{\partial X}\right) \text{ or } \mathrm{Nu}_{\mathrm{Local}^{\mathrm{hb}}} = \frac{k_{\mathrm{eff}}}{k_{\mathrm{f}}}\left(\frac{\partial\theta_{\mathrm{p}}}{\partial Y}\right). \tag{2.18}$$

Local Nusselt number at the portion of the inner heated rectangular cavity lies in the clear fluid layer:

$$\mathrm{Nu}_{\mathrm{Local}^{\mathrm{hb}}} = \frac{k_{\mathrm{hnf}}}{k_{\mathrm{f}}}\left(\frac{\partial\theta_{\mathrm{hnf}}}{\partial X}\right) \text{ or } \mathrm{Nu}_{\mathrm{Local}^{\mathrm{hb}}} = \frac{k_{\mathrm{hnf}}}{k_{\mathrm{f}}}\left(\frac{\partial\theta_{\mathrm{hnf}}}{\partial Y}\right). \tag{2.19}$$

The “average Nusselt number” at the inner heated rectangular cavity ($\mathrm{Nu}_{\mathrm{avg}^{\mathrm{hb}}}$) is determined by using the formula defined in the following equation:

$$\begin{aligned} \mathrm{Nu}_{\mathrm{avg}^{\mathrm{hb}}} = {} & \frac{1}{0.25}\left(\frac{k_{\mathrm{eff}}}{\mathrm{k_f}}\right)\int_{0.25}^{0.50}\left(\frac{\partial\theta_{\mathrm{p}}}{\partial X}\right)_{X=0.4}\mathrm{d}Y \\ & + \frac{1}{0.25}\left(\frac{k_{\mathrm{hnf}}}{k_{\mathrm{f}}}\right)\int_{0.50}^{0.75}\left(\frac{\partial\theta_{\mathrm{hnf}}}{\partial X}\right)_{X=0.4}\mathrm{d}Y \\ & + \frac{1}{0.25}\left(\frac{k_{\mathrm{eff}}}{k_{\mathrm{f}}}\right)\int_{0.25}^{0.50}\left(\frac{\partial\theta_{\mathrm{p}}}{\partial X}\right)_{X=0.6}\mathrm{d}Y \\ & + \frac{1}{0.25}\left(\frac{k_{\mathrm{hnf}}}{k_{\mathrm{f}}}\right)\int_{0.50}^{0.75}\left(\frac{\partial\theta_{\mathrm{hnf}}}{\partial X}\right)_{X=0.6}\mathrm{d}Y \\ & + \frac{1}{0.2}\left(\frac{k_{\mathrm{eff}}}{k_{\mathrm{f}}}\right)\int_{0.40}^{0.60}\left(\frac{\partial\theta_{\mathrm{p}}}{\partial Y}\right)_{Y=0.25}\mathrm{d}X \\ & + \frac{1}{0.2}\left(\frac{k_{\mathrm{hnf}}}{k_{\mathrm{f}}}\right)\int_{0.40}^{0.60}\left(\frac{\partial\theta_{\mathrm{hnf}}}{\partial Y}\right)_{Y=0.75}\mathrm{d}X. \end{aligned} \tag{2.20}$$

3 Numerical solution methodology

Several advanced numerical techniques have been designed to decode the complexities of fluid flow and heat transfer dynamics within the cavity. This investigation utilizes the finite difference discretization method to discretize governing Eqs. (2.10)–(2.12) in association with respective BCs. The resulting discretized equations are as follows:

$$\begin{aligned} & \frac{1}{h^2}(\psi_{\mathrm{p,hnf}(i+1,j)} + \psi_{\mathrm{p,hnf}(i-1,j)} - 4\psi_{\mathrm{p,hnf}(i,j)} \\ & \quad + \psi_{\mathrm{p,hnf}(i,j+1)} + \psi_{\mathrm{p,hnf}(i,j-1)}) = -\omega_{\mathrm{p,hnf}(i,j)}, \end{aligned} \tag{3.1}$$

$$\begin{aligned} & \left(\frac{1}{4h^2}\right)\Big((\psi_{\mathrm{p,hnf}(i,j+1)} - \psi_{\mathrm{p,hnf}(i,j-1)})(\omega_{\mathrm{p,hnf}(i+1,j)} \\ & \quad - \omega_{\mathrm{p,hnf}(i-1,\ j)})\Big) \\ & \quad - \left(\frac{1}{4h^2}\right)\Big((\psi_{\mathrm{p,hnf}(i+1,j)} - \psi_{\mathrm{p,hnf}(i-1,j)})(\omega_{\mathrm{p,hnf}(i,j+1)} \\ & \quad - \omega_{\mathrm{p,hnf}(i,j-1)})\Big) \\ & = \varepsilon\mathrm{Pr}\left(\frac{\mu_{\mathrm{hnf}}}{\mu_{\mathrm{f}}}\right)\left(\frac{\rho_{\mathrm{f}}}{\rho_{\mathrm{hnf}}}\right)\left(1 + \frac{1}{\gamma}\right)\left(\frac{1}{h^2}\right)\Big(\omega_{\mathrm{p,hnf}(i+1,j)} \\ & \quad + \omega_{\mathrm{p,hnf}(i-1,j)} - 4\omega_{\mathrm{p,hnf}(i,j)} + \omega_{\mathrm{p,hnf}(i,j+1)} \\ & \quad + \omega_{\mathrm{p,hnf}(i,j-1)}\Big) - \left(\frac{\mu_{\mathrm{hnf}}}{\mu_{\mathrm{f}}}\right)\left(\frac{\rho_{\mathrm{f}}}{\rho_{\mathrm{hnf}}}\right)\delta\varepsilon^2\frac{\mathrm{Pr}}{\mathrm{Da}}\omega_{\mathrm{p,hnf}(i,j)} \\ & \quad + \frac{(\rho\beta)_{\mathrm{hnf}}}{\rho_{\mathrm{hnf}}\beta_{\mathrm{f}}}\varepsilon^{2}\ \mathrm{PrRa}\left(\frac{1}{2h}\right)(\theta_{i+1,j} - \theta_{i-1,j}) \\ & \quad + \mathrm{Ha}^2\mathrm{Pr}\varepsilon^2\left(\frac{\sigma_{\mathrm{hnf}}}{\sigma_{\mathrm{f}}}\right)\left(\frac{\rho_{\mathrm{f}}}{\rho_{\mathrm{hnf}}}\right)\left(\frac{1}{h^2}\right)\Big(\psi_{\mathrm{p,hnf}(i+1,j)} - 2\psi_{\mathrm{p,hnf}(i,j)} \\ & \quad + \psi_{\mathrm{p,hnf}(i-1,j)}\Big), \end{aligned} \tag{3.2}$$

$$\begin{aligned} & \left(\frac{1}{4h^2}\right)\Big((\psi_{\mathrm{p,hnf}(i,j+1)} - \psi_{\mathrm{p,hnf}(i,j-1)})(\theta_{\mathrm{p,hnf}(i+1,j)} \\ & \quad - \theta_{\mathrm{p,hnf}(i-1,j)})\Big) - \left(\frac{1}{4h^2}\right)\Big((\psi_{\mathrm{p,hnf}(i+1,j)} \\ & \quad - \psi_{\mathrm{p,hnf}(i-1,j)})(\theta_{\mathrm{p,hnf}(i,j+1)} - \theta_{\mathrm{p,hnf}(i,j-1)})\Big) \\ & = \left(\frac{\alpha^*}{\alpha_{\mathrm{f}}}\right)\left(\frac{1}{h^2}\right)\Big(\theta_{\mathrm{p,hnf}(i+1,j)} + \theta_{\mathrm{p,hnf}(i-1,j)} - 4\theta_{\mathrm{p,hnf}(i,j)} \\ & \quad + \theta_{\mathrm{p,hnf}(i,j+1)} + \theta_{\mathrm{p,hnf}(i,j-1)}\Big). \end{aligned} \tag{3.3}$$

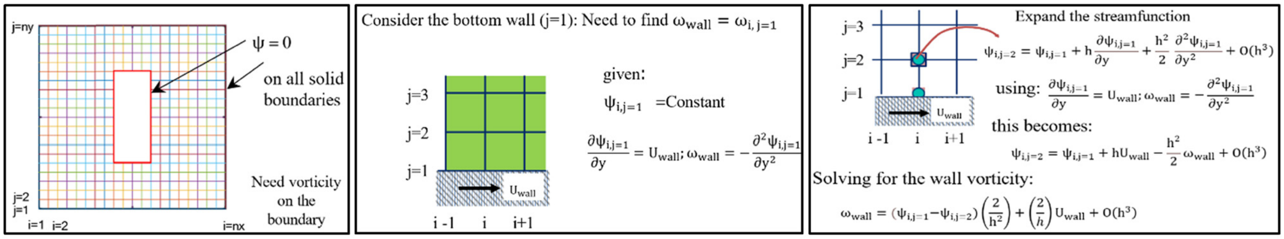

(a) (b) (c)

Figure 2: Calculation procedure for vorticity at solid walls as explained in steps (a), (b) and (c).

Here, i and j denote the node points in x and y directions, respectively, and h is the grid space in x and y directions.

The diffusion terms are estimated using second-order central differencing, while the upwind scheme was implemented for controlling the convective terms in the temperature and linear momentum equations. These equations serve as a foundation for calculating the solution at the interior points of the computational domain. Furthermore, a detailed methodology for calculating the vorticity at the solid walls of the enclosure and the heated rectangular cavity has been included and depicted in Figure 2(a)–(c). This detailed approach ensures accuracy in capturing the BCs and enhances the overall numerical framework. The resulting difference equations (Eqs. (3.1)–(3.3)) together with BCs, as illustrated in Figure 2, are computationally solved employing finite difference method in combination with iterative techniques. Specifically, the successive over relaxation method is utilized for the Poison equation, the under relaxation method is utilized for the vorticity, and the Gauss–Seidel method is employed to solve the energy equation. Iterations continued until the condition $\frac{\sum_{i,j}|\varphi_{i,j}^{k+1} - \varphi_{i,j}^{k}|}{\sum_{i,j}|\varphi_{i,j}^{k+1}|} \le 10^{-7}$ was satisfied, where φ stands for any measured value from ψ, ω, and θ. The simulation was carried out over a maximum of 10^4 iterations, requiring approximately 11 min of CPU time, allowing a residual error threshold of 10^{-7}. Furthermore, Figure 3 has been included to provide a clear visualization of the residual error trend with the number of iterations across these numerical techniques. Also, a flow chart of the computational program, offering a clear overview of the problem-solving process, is

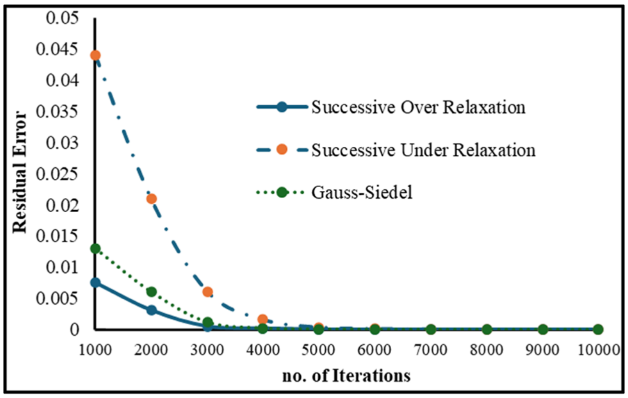

Figure 3: Residual error plotted against the number of iterations for various numerical techniques.

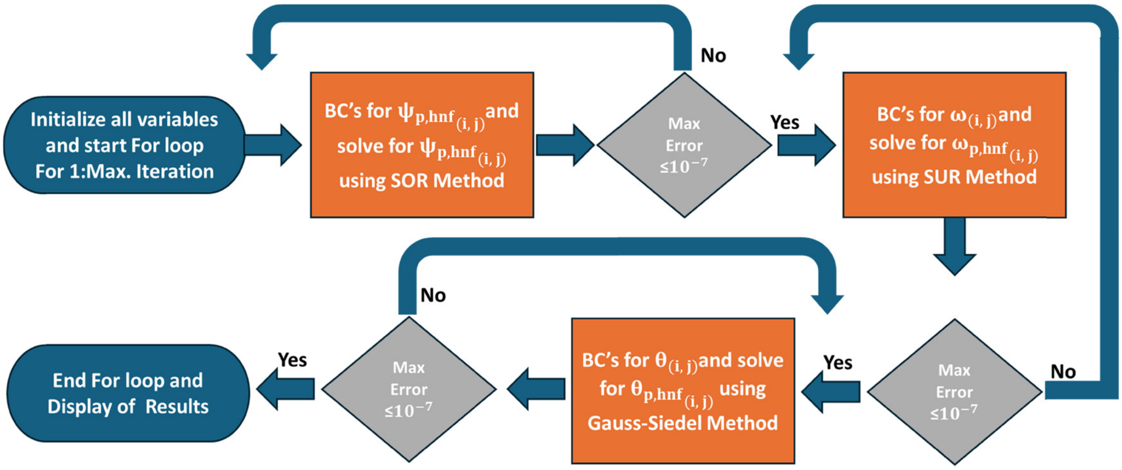

Figure 4: Flow chart of the solution procedure.

given in Figure 4. Computational calculations were carried out by utilizing the especially self-developed MATLAB code. The accuracy of self-developed codes was verified using a specific outcome of Chamkha and Ismael [41] and Jani *et al.* [42]. Figure 5(a) exhibits a comparison of the streamlines and isotherm contours produced by self-developed in-house MATLAB programs with the findings of Chamkha and Ismael [41] and Figure 5(b), local Nusselt number variation is examined with outcomes of Jani *et al.* [42]. The excellent correlation between the outcomes confirms the validity of our simulation. The grid independency of the self-developed codes was examined by computing average Nusselt number and given in Table 2. Hence, in order to obtain the required results, the 101 × 101 grids are used.

Table 2: Average Nusselt number at heat flux ($\mathrm{Nu}_{\mathrm{avg}^{\mathrm{hf}}}$) and heated rectangular block ($\mathrm{Nu}_{\mathrm{avg}^{\mathrm{hb}}}$) to check the grid independency of codes when $\mathrm{Da} = 10^{-3}$, $\mathrm{Ra} = 10^{5}$, $\mathrm{Ha} = 5$, $\gamma = 0.5$, $\varepsilon = 0.398$, $K_i = 1.0$, $N = 4$, $\mathrm{Pr} = 6.26$, $\phi_{\mathrm{hnf}} = 0.04$

Grid size	81 × 81	101 × 101	121 × 121	141 × 141
$\mathrm{Nu}_{\mathrm{avg}^{\mathrm{hf}}}$	1.0328	1.0591	1.0585	1.0584
$\mathrm{Nu}_{\mathrm{avg}^{\mathrm{hb}}}$	19.6635	19.9259	19.9248	19.9242

4 Results and discussion

In the present study, the impacts of a sinusoidal heat flux and a heated rectangular cavity in a partially porous Casson hybrid nanofluid-filled square enclosure being affected by a constant magnetic field imposed in the x-direction having magnitude B_0 on natural convection were investigated numerically. Numerical calculations were carried out using the values of the calibrated parameters in the range $0 \le \mathrm{Ha} \le 10$, $10^4 \le \mathrm{Ra} \le 10^6$, $0.00 \le \phi_{\mathrm{hnf}} \le 0.04$, $10^{-5} \le \mathrm{Da} \le 10^{-3}$, $0.1 \le \gamma \le 1$, and $4 \le N \le 12$.

4.1 Effects of pertinent parameters on streamlines and isotherms

In Figure 6, the influence of buoyancy force on the thermal and flow profiles is depicted when the other parameters were fixed at $\mathrm{Da} = 10^{-3}$, $\mathrm{Ha} = 5$, $\phi_{\mathrm{hnf}} = 0.04$, $\gamma = 0.5$, $K_i = 1$, $N = 4$. The results show that the appearance of a centrally positioned rectangular heated cavity within the enclosure

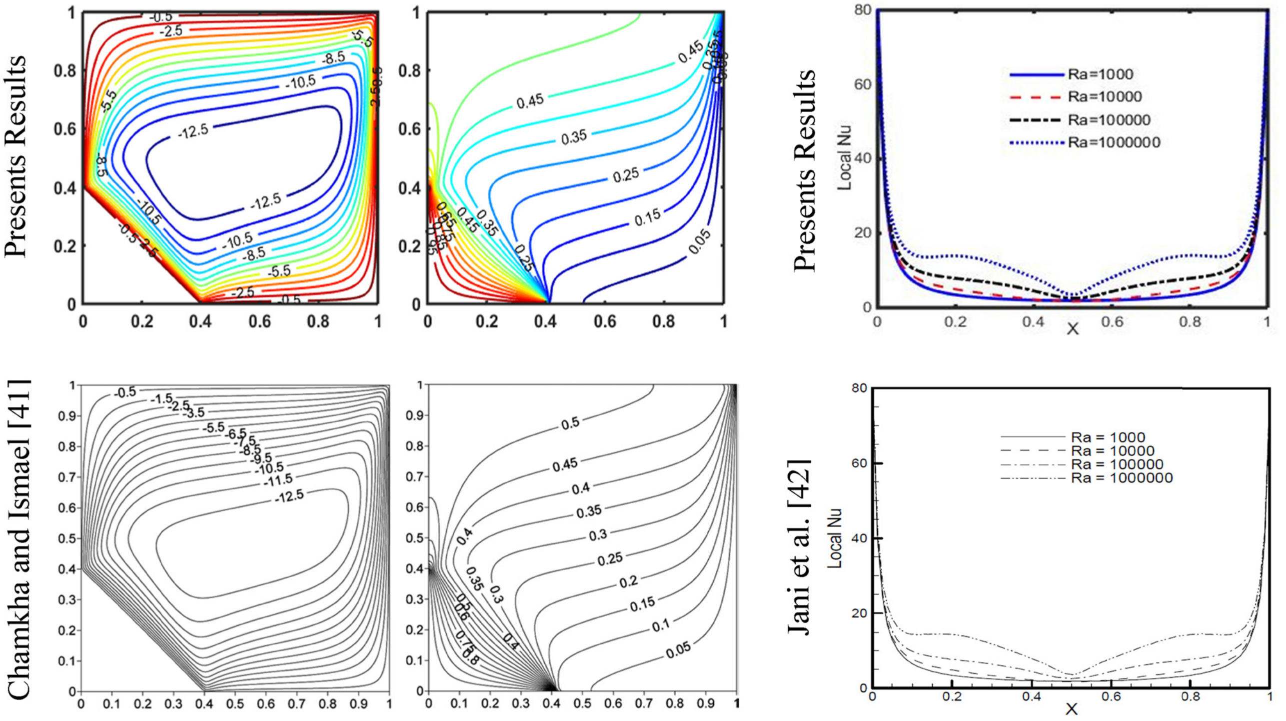

(a) (b)

Figure 5: Validation of self-developed MATLAB codes with specific outcomes of Chamkha and Ismael [41] (a) at Ra = 800 and Kr = 1 and with Jani *et al.* [42] (b), at different Rayleigh number (Ra) with Ha = 0.

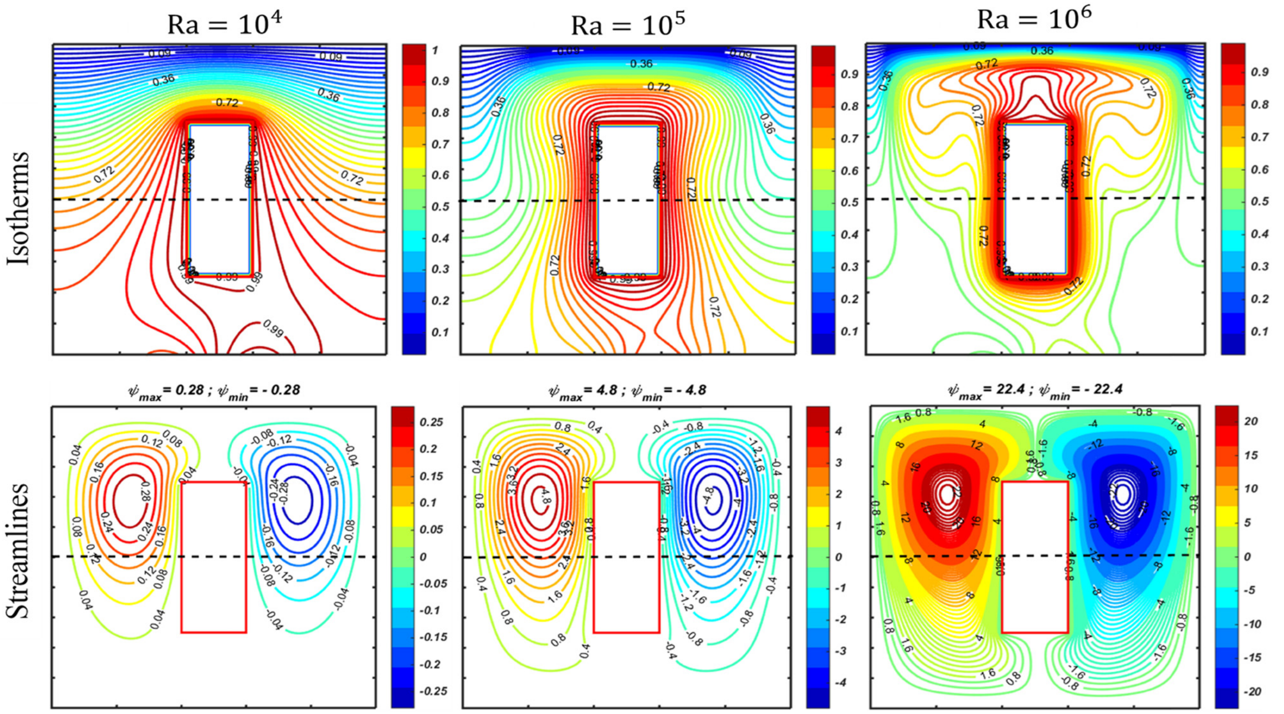

Figure 6: Impact of Ra on a pattern of streamlines and isotherms when Da = 10^{-3}, Ha = 5, ϕ_{hnf} = 0.04, ε = 0.398, γ = 0.5, K_i = 1.0, N = 4, Pr = 6.26.

results in the development of two symmetrical circulation cells. These cells exhibit clockwise and anticlockwise rotation in all situations. Physically, the Rayleigh number measures the balance between thermal buoyancy and viscous forces. A low Rayleigh number indicates weak buoyancy relative to viscous and thermal diffusion effects, resulting in more orderly, subdued streamlines and smoother, less pronounced isotherms. However, an increase in Ra improves buoyancy-assisted flow that leads to an intensification of fluid circulation in the clear-fluid and porous regions. Therefore, as Ra rises from 10^4 to 10^6, the clockwise and counterclockwise vortex cells are both magnified in size and strength. The ψ_{max} increases from 0.28 to 22.4 as Ra upsurges from 10^4 to 10^6. The contours of the isotherms depicted in Figure 6 illustrate the impacts of Ra on a natural convection phenomenon. The dominance of heat transfer through conduction is demonstrated by the smoothness of the isotherms at small Rayleigh numbers, *i.e.*, Ra = 10^4. Whereas, at Ra = 10^6 the isotherms become more irregular and skewed, reflecting increased thermal gradients and complex convective patterns. Hence, buoyancy force is clearly dominant over viscous forces, as evidenced by strong isotherms, and heat transfer occurs *via* convection. As Ra rises from 10^4 to 10^6, convective heat transfer continues to dominate, and the higher temperature zone has squeezed in the enclosure around the rectangular heated cavity, enhancing the temperature differences and the average Nusselt number on the rectangular heated cavity. In the porous layer, the increase of Ra manifests a diminution in the hot region and amplification of the convective heat transfer. Whereas in the fluid region, the isotherms form a plum-like structure above the heated cavity, and more bending toward the implanted heated rectangular cavity is observed as Ra rises to a value of 10^6. Natural convection intensification caused the isotherms to become symmetrical about the vertical midline of the square cavity at Ra = 10^6.

Figure 7 depicts flow and temperature variation profiles within the cavity with respect to the Ha. The streamlines were substantially influenced by the Ha. If the magnetic field is applied, the velocity profiles experience a type of resisting force known as the Lorentz force. As a result, the resisting force increases simultaneously with Ha, leading to a consistent decrease in velocity. This suppression appears in the streamline profiles as more aligned, subdued flow patterns with reduced circulation and weaker vortices. At low Ha values, the streamlines exhibit more pronounced and dynamic circulation, indicating stronger convection currents. However, as Ha increases, the flow becomes more damped, and the streamlines shift toward a more uniform, layered structure, reflecting the dominant influence of the magnetic field in stabilizing the flow and reducing fluid motion across the domain. This damping effect is crucial in applications controlling or

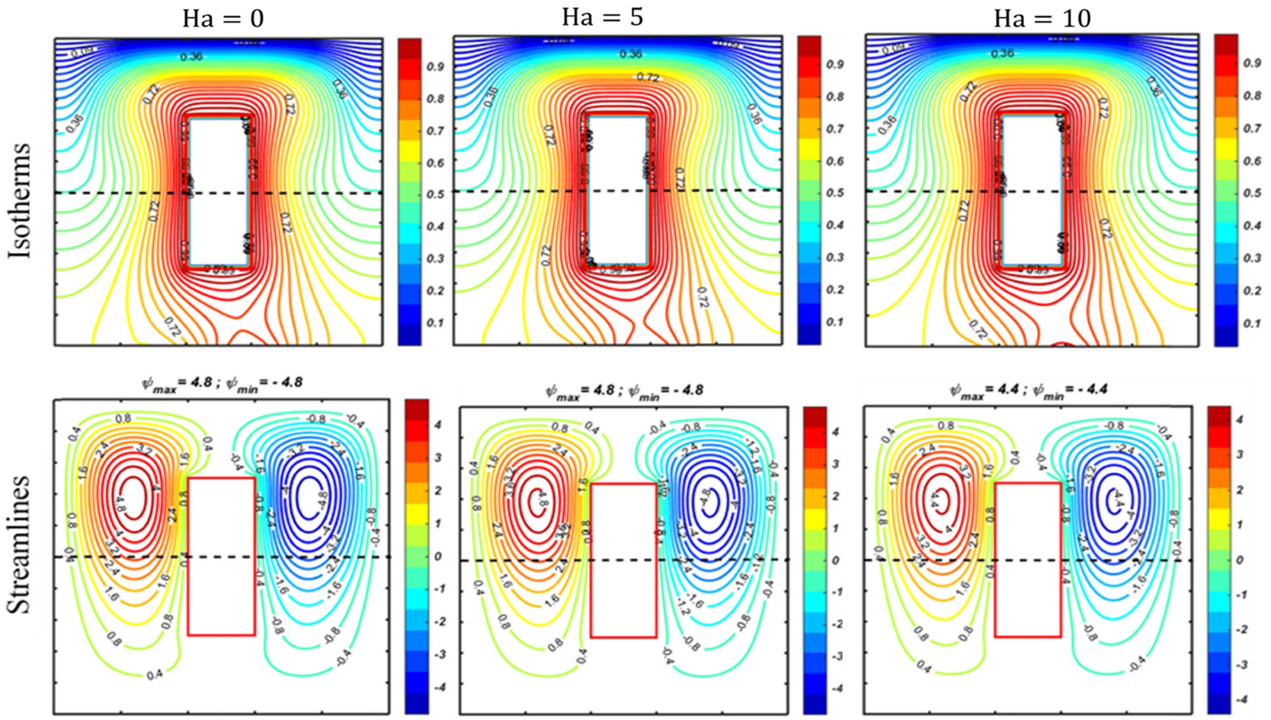

Figure 7: Impact of Ha on a pattern of streamlines and isotherms when Da = 10^{-3}, Ra = 10^5, $\phi_{\mathrm{hnf}} = 0.04$, $\varepsilon = 0.398$, $\gamma = 0.5$, $K_i = 1.0$, $N = 4$, $\Pr = 6.26$.

reducing fluid movement, such as in magnetic damping systems or flow control in engineering processes. These findings are consistent with the outcomes of Malvandi *et al.* [43]. So, as the magnetic field rises, the flow as well as circulation decelerated and $\psi_{\max}$ falls from 4.8 to 4.4 as Ha rises from 0 to 10. Furthermore, the isotherms close to the heat flux at centrally located bottom wall are slightly affected by magnetic field strength, whereas in the clear fluid region of the cavity, Ha has no significant effect on isotherms lines. It can be determined quantitatively in light of heat transfer from heat flux and embraced heated rectangular cavity. Enhancement in Ha increases isotherm concentration, which in turn decreases natural convection and increases fluid temperature.

Figure 8 explores how the permeability of the porous medium, as characterized by the Darcy number (Da), influences fluid flow and heat transfer. Physically, a high Darcy number indicates high permeability, allowing for easier fluid flow through the porous medium. This results in streamlines that appear more streamlined and less obstructed, with isotherms showing smoother, more uniform thermal distribution. The value of $\psi_{\max}$ decreases from 4.8 to 4.4 as the value of Da decreases from 10^{-3} to 10^{-5}. It is clear from Figure 8 that a higher value for Da increases the permeability of the porous layer, allowing more fluid to penetrate the porous layer and thus intensifying the vortex cell's strength. The results obtained are in proportionate with the findings reported by Chamkha and Ismael [40]. In contrast to the outcomes at a lower value of Da = 10^{-5}, isotherm contours around the embraced rectangular heated cavity are denser compared to when Da = 10^{-3}. The porous medium's permeability was reported to decrease as the Da decreases; therefore, with the decrease in Da, a higher temperature zone has formed near the rectangular heated cavity, *i.e.*, fluid retains more heat, leading to a rise in fluid's temperature in the porous region and a significant decline in heat convection from both heat flux and embraced rectangular heated cavity. Enhancing Da improves heat convection rate, as evidenced by the relatively flat isotherms for the region of clear fluid and supported by the quantitative data tabulated in Table 3. It is worth noting that the current Casson fluid model simplifies to the Newtonian fluid model as "Casson fluid parameter, *i.e.*, $\gamma \to \infty$." For $\gamma = 0.1$, 0.5, and 1, the streamline and isotherms are shown in Figure 9.

Higher values of γ indicate an abatement in the effective viscosity of the Casson nanofluid, causing an escalation in the velocity; as a result, the amplitude of the stream function is enhanced. Also, it is noticed that a surge in γ supports to densification of the streamlines. The value of $\psi_{\max}$ increases from 0.8 to 6.4 as the value of Casson parameter (γ) increases from 0.1 to 1. The outcomes of this investigation are supported by the findings of Ganesh *et al.* [33]. On isotherm profiles, the effects of γ are precisely

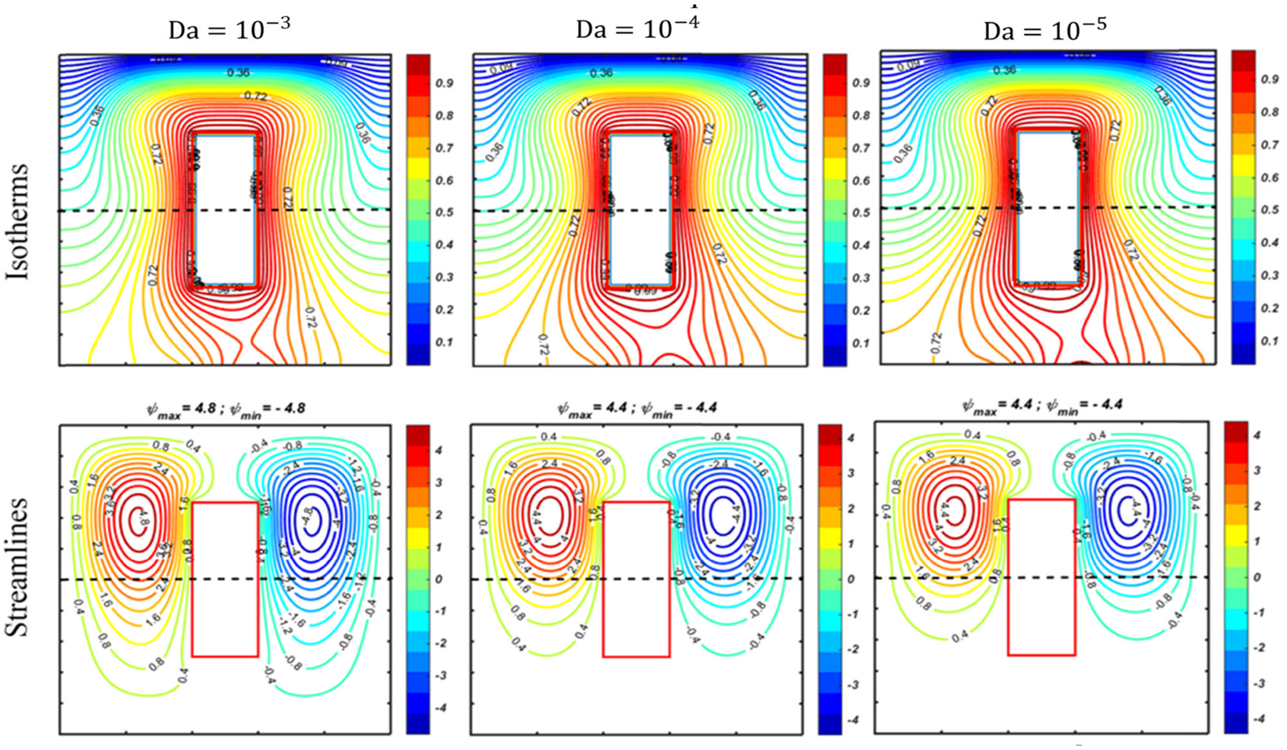

Figure 8: Impact of Da on the pattern of streamlines and isotherms when Ra = 10^5, Ha = 5, ϕ_{hnf} = 0.04, ε = 0.398, γ = 0.5, K_i = 1.0, N = 4, Pr = 6.26.

identical to the effects of the Ra. At γ = 0.1, the isotherms are flattening out, suggesting that most of the heat is transferred by conduction. The hot region in the porous layer reduces with the rise in Casson parameter γ, which leads to an improvement in heat transfer through convection. As it is well known, increasing the value of the Casson parameter, *i.e.*, γ, causes the fluid's viscosity to decrease, resulting in a rise in heat convection.

Table 3: Effect of parameters and AR of a rectangular heated cavity on average Nusselt number calculated at heat flux ($\mathrm{Nu}_{\mathrm{avg}^{\mathrm{hf}}}$) and at a heated rectangular cavity ($\mathrm{Nu}_{\mathrm{avg}^{\mathrm{hb}}}$)

Ra	Da	Ha	γ	ϕ_{hnf}	N	$\mathrm{Nu}_{\mathrm{avg}^{\mathrm{hf}}}$ (AR = 2/5)	$\mathrm{Nu}_{\mathrm{avg}^{\mathrm{hb}}}$ (AR = 2/5)	$\mathrm{Nu}_{\mathrm{avg}^{\mathrm{hf}}}$ (AR = 1/6)	$\mathrm{Nu}_{\mathrm{avg}^{\mathrm{hb}}}$ (AR = 1/6)
10^5	10^{-3}	5	0.5	0.04	4	1.0591	19.9259	1.1616	22.3020
10^3	10^{-3}	5	0.5	0.04	4	0.8511	12.9091	0.8720	16.2572
10^4	10^{-3}	5	0.5	0.04	4	0.8578	12.9335	0.8851	16.4556
10^6	10^{-3}	5	0.5	0.04	4	1.5017	44.0016	1.5249	44.6247
10^5	10^{-1}	5	0.5	0.04	4	1.1278	20.2330	1.2463	23.2339
10^5	10^{-2}	5	0.5	0.04	4	1.1184	20.1908	1.2352	23.1062
10^5	10^{-4}	5	0.5	0.04	4	0.9842	19.4858	1.0571	21.1820
10^5	10^{-3}	0	0.5	0.04	4	1.0645	20.1762	1.1672	22.5222
10^5	10^{-3}	10	0.5	0.04	4	1.0435	19.2288	1.1450	21.6883
10^5	10^{-3}	15	0.5	0.04	4	1.0193	18.2225	1.1180	20.7978
10^5	10^{-3}	5	0.01	0.04	4	0.8527	12.9072	0.8752	16.2129
10^5	10^{-3}	5	0.1	0.04	4	0.8874	13.5078	0.9472	16.7219
10^5	10^{-3}	5	1	0.04	4	1.1189	23.0881	1.2185	24.7418
10^5	10^{-3}	5	0.5	0.00	4	1.0500	19.5626	1.1462	21.4740
10^5	10^{-3}	5	0.5	0.02	4	1.0550	19.7623	1.1545	21.8929
10^5	10^{-3}	5	0.5	0.06	4	1.0625	20.0599	1.1675	22.7051
10^5	10^{-3}	5	0.5	0.08	4	1.0722	21.4299	1.1721	23.1090
10^5	10^{-3}	5	0.5	0.04	8	1.0550	19.9128	1.1107	21.6158
10^5	10^{-3}	5	0.5	0.04	12	1.0548	19.9078	1.1483	22.1571

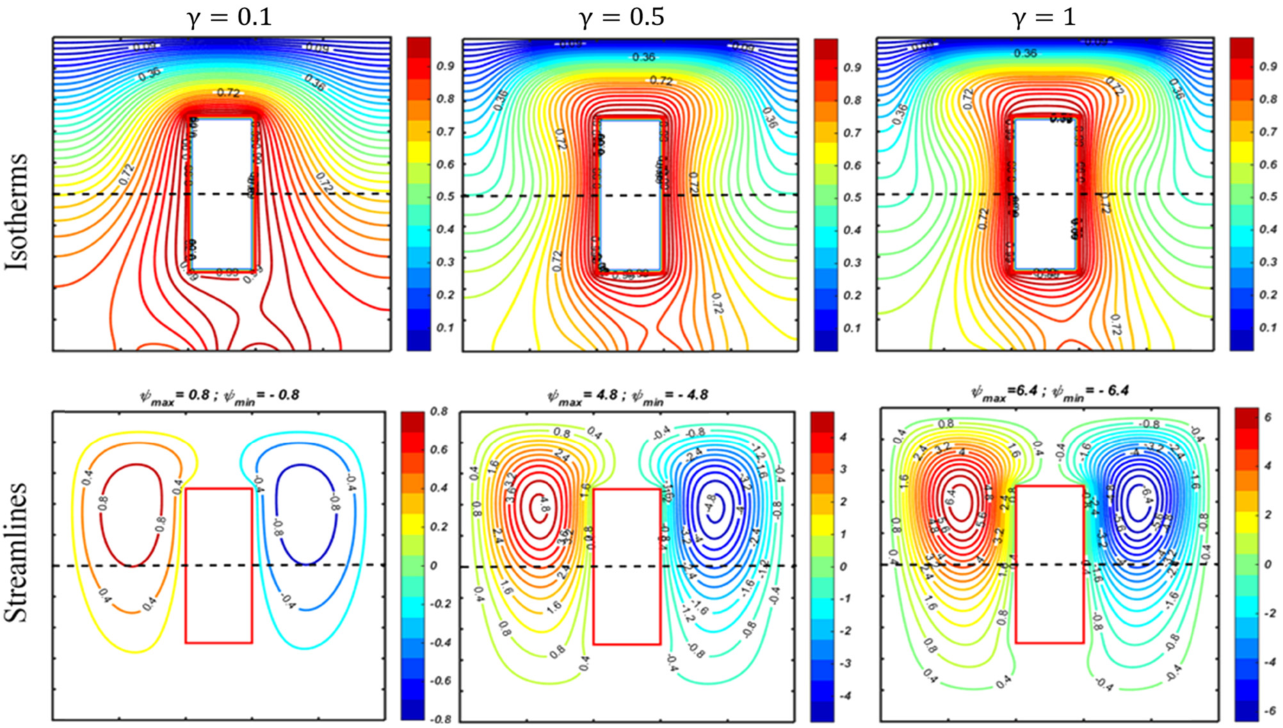

Figure 9: Effect of γ on streamlines and isotherms when Da = 10^{-3}, Ha = 5, ϕ_{hnf} = 0.04, ε = 0.398, Ra = 10^5, K_i = 1.0, N = 4, Pr = 6.26.

Figure 10 explores the impact of solid nanoparticle volume concentration (ϕ_{hnf}) on the streamlines as well as on isotherms. Incorporation of Cu–Al_2O_3 hybrid nanoparticles into the base fluid, profoundly affects both the streamlines and the isotherms. There is a considerable reduction in the stream function (ψ) strength as ϕ_{hnf} increases up to 8%. This reduction in ψ is triggered by a rise in flow resistance which is a consequence of the incorporation of nanoparticles to the base fluid. The $\psi_{\max}$ is reduced from 5.2 to 4.4 as the value of ϕ_{hnf} rises from 0 to 8%. The isotherms experience significant changes with an upsurge in ϕ_{hnf}, as illustrated in Figure 10. It is discovered that enhancing in ϕ_{hnf} leads to a decrease in the level of compactness exhibited by the isotherms surrounding the encapsulated rectangular heated cavity; therefore, heat convection is improved. The incorporation of nanoparticles causes a reduction in the temperature difference in the fluid, particularly just above the rectangular heated cavity. In order to explore the impact of N on the heat convection process and fluid flow properties, Figure 11 is plotted for N = 4, 8, and 12. Figure 11 shows that varying the value of N, there were no significant changes on the streamlines, while isotherms are changed significantly near the heat flux in the porous region but nearly unchanged in the clear fluid region. An increase in N slightly enlarges the hot zone in the porous region; consequently, the temperature difference decreases in the porous region, especially just below the rectangular heated cavity, and more heat is trapped in the porous region, resulting in a decrease in the heat convection rate.

Figure 12 illustrates the effect of the aspect ratio (AR) of a rectangular heated cavity on streamlines and isotherms within the partially porous enclosure, with all other parameters set at Ha = 5, Da = 10^{-3}, N = 4, γ = 0.5, ε = 0.398, Ra = 10^5, K_i = 1.0, ϕ_{hnf} = 0.04, Pr = 6.26. The AR significantly influences the behavior of streamlines and isotherms within the porous cavity. For instance, when the aspect ratio is AR = 1/6, we observe a dense arrangement of isotherms, forming a plume-like structure in the fluidic region adjacent to the heated rectangular cavity. This configuration indicates enhanced flow circulation and heat transfer due to the increased fluid entry into the porous region. In contrast, as the aspect ratio increases to AR = 3/4, the curvature and compactness of the isotherms diminish. This reduction is indicative of restricted flow circulation and a reduced entry of fluid into the porous region, leading to diminished heat transfer. Consequently, the thermal boundary layer thickness also increases, which results in more heat being trapped near the heated wall and within the porous medium, further contributing to decreased heat transfer efficiency. The changes in the $\mathrm{Nu}_{\mathrm{Local}}{}^{\mathrm{hf}}$ with respect to the calibrated parameters Ha, Ra, Da, N, ϕ_{hnf}, and γ are depicted in Figure 13. The $\mathrm{Nu}_{\mathrm{Local}}{}^{\mathrm{hf}}$ has a sinusoidal curve profile.

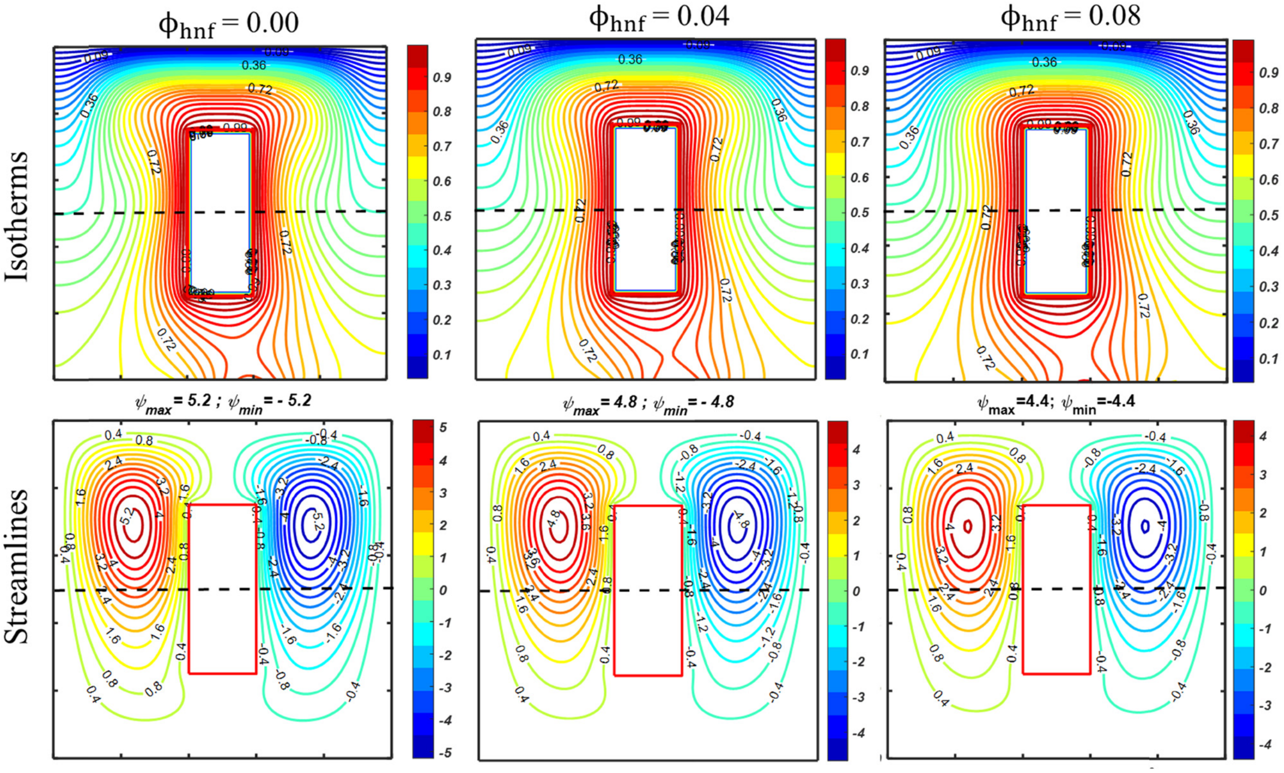

Figure 10: Impact of ϕ_{hnf} on the pattern of streamlines and isotherms when Da = 10^{-3}, Ha = 5, $\gamma = 0.5$, $\varepsilon = 0.398$, Ra = 10^5, $K_i = 1.0$, $N = 4$, $\mathrm{Pr} = 6.26$.

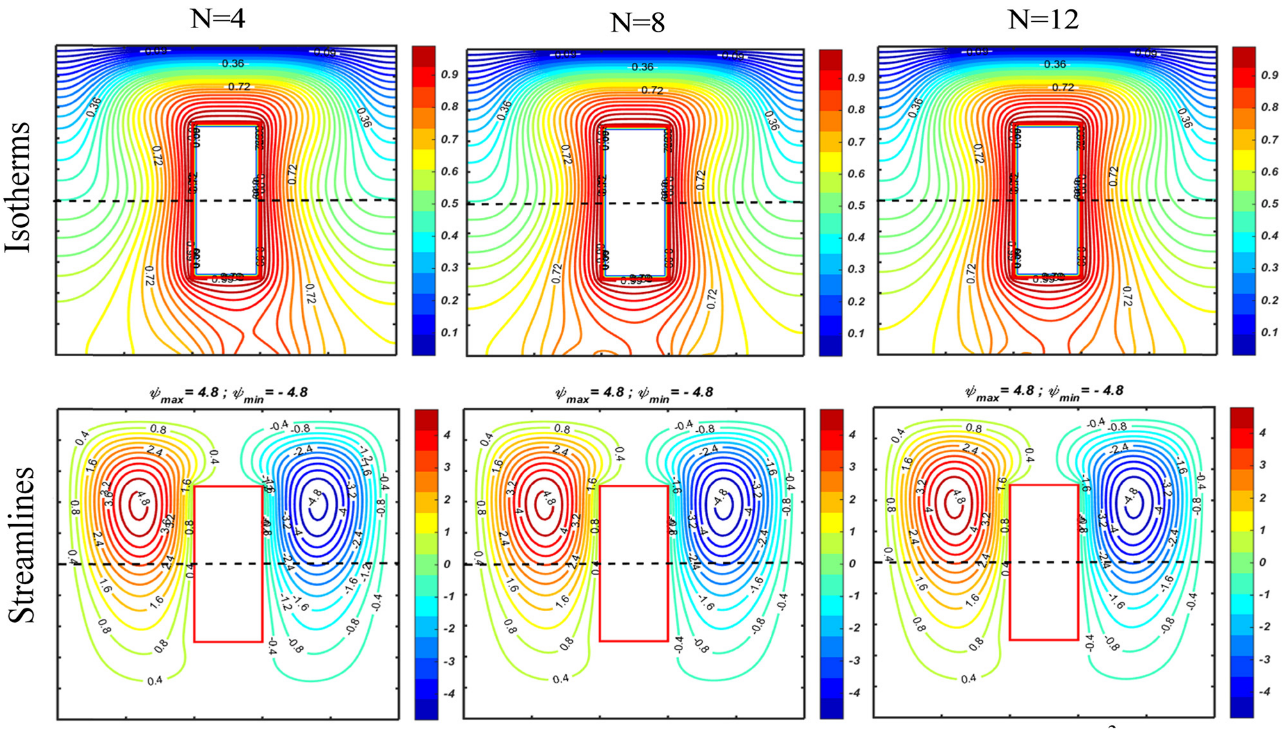

Figure 11: Impact of N on the pattern of streamlines and isotherms when Da = 10^{-3}, Ha = 5, $\gamma = 0.5$, $\varepsilon = 0.398$, Ra = 10^5, $K_i = 1.0$, $\phi_{\mathrm{hnf}} = 0.04$, $\mathrm{Pr} = 6.26$.

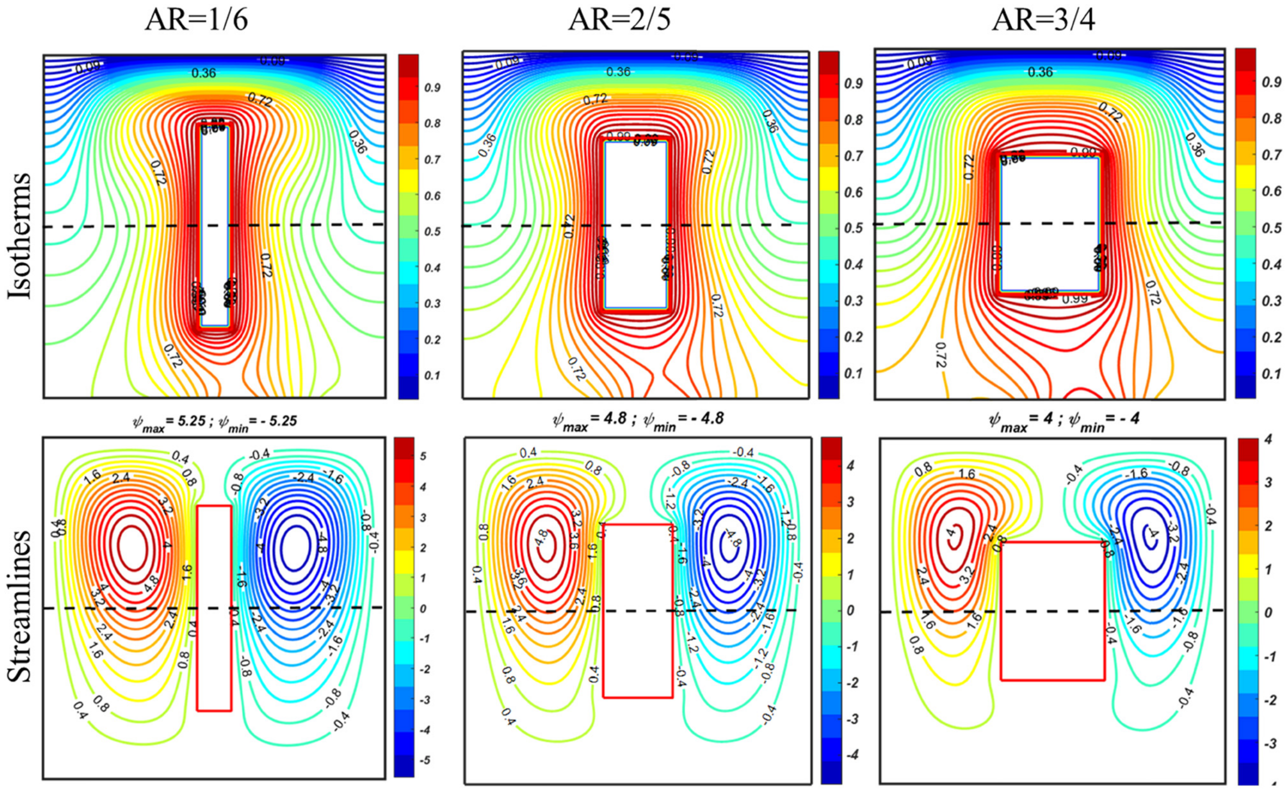

Figure 12: Impact of AR on the pattern of streamlines and isotherms when Ha = 5, Da = 10^{-3}, N = 4, γ = 0.5, ε = 0.398, Ra = 10^5, K_i = 1.0, ϕ_{hnf} = 0.04, Pr = 6.26.

4.2 Effects of pertinent parameters on average Nusselt number

In Figures 14–17, the average Nusselt number at centrally located heat flux ($\mathrm{Nu_{avg}}^{\mathrm{hf}}$) at the bottom wall and the rectangular heated cavity ($\mathrm{Nu_{avg}}^{\mathrm{hb}}$) is examined. Figure 14 illustrates the impact of Da and ϕ_{hnf} on $\mathrm{Nu_{avg}}^{\mathrm{hf}}$ and $\mathrm{Nu_{avg}}^{\mathrm{hb}}$ with varying γ.

It is observed that with increasing γ, both $\mathrm{Nu_{avg}}^{\mathrm{hf}}$ and $\mathrm{Nu_{avg}}^{\mathrm{hb}}$ improve significantly for all the considered values of Da and ϕ_{hnf}. Also, it has been found that $\mathrm{Nu_{avg}}$hf and $\mathrm{Nu_{avg}}^{\mathrm{hb}}$ drop substantially as the Da decreases; however, as

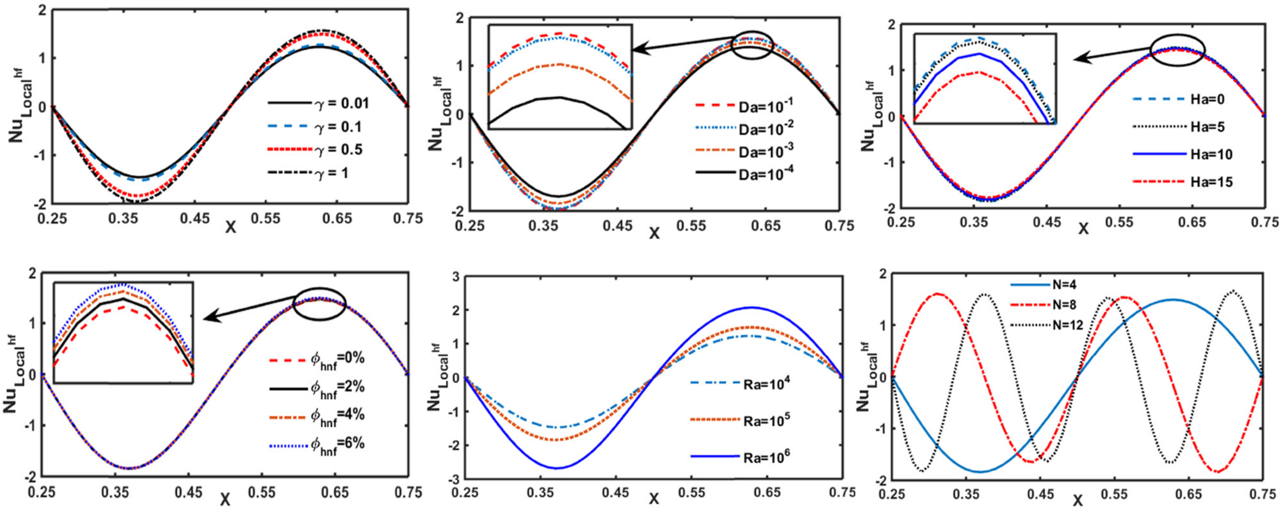

Figure 13: Variation in local Nusselt number ($\mathrm{Nu_{Local^{hf}}}$) at heat flux with various parameters.

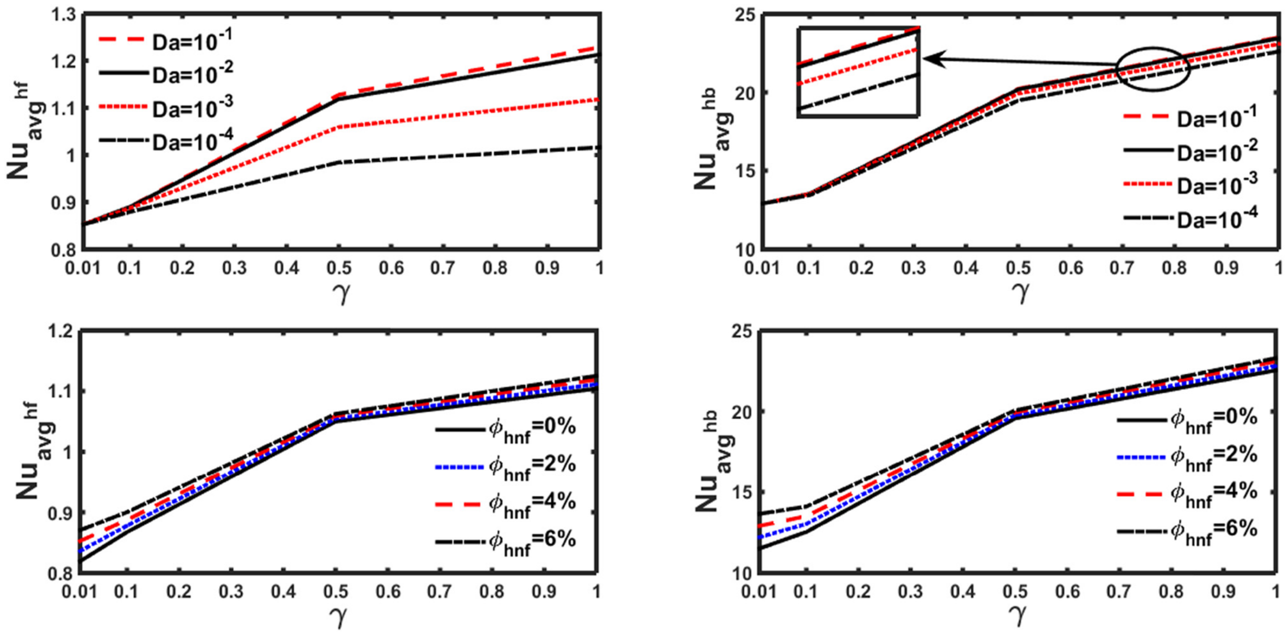

Figure 14: Influence of Da and ϕ_{hnf} on $\mathrm{Nu_{avg}}^{\mathrm{hf}}$ and $\mathrm{Nu_{avg}}^{\mathrm{hb}}$ with variation in 'γ'.

$\gamma > 0.5$, this decline becomes consistent. With the reduction in Da, there is an observable attenuation in $\mathrm{Nu_{avg}}$hf in comparison to $\mathrm{Nu_{avg}}^{\mathrm{hb}}$. Whereas the average Nusselt number increases with a growing ϕ_{hnf}, but this effect is more substantial for a lower value of γ compared to large ones, as depicted in Figure 14. According to the data summarized in Table 3, decreasing the Da from 10^{-1} to 10^{-4}, $\mathrm{Nu_{avg}}^{\mathrm{hf}}$ reduces by 12.73%, whereas a 3.69% reduction is observed in $\mathrm{Nu_{avg}}^{\mathrm{hb}}$; on the other hand, 1.19 and 2.54% increment in $\mathrm{Nu_{avg}}^{\mathrm{hf}}$ and $\mathrm{Nu_{avg}}^{\mathrm{hb}}$ is reported as ϕ_{hnf} rises from 0 to 6%, at a fixed value of $\gamma = 0.5$ and AR = 2/5. Buoyancy-assisted flow is enhanced as the Ra rises. Consequently, the average Nusselt number at heat flux and rectangular heated cavity is improved with the improvement of Ra, as depicted in Figure 15.

It is found that for any given value of Ra, raising γ results in a considerable improvement in both $\mathrm{Nu_{avg}}^{\mathrm{hf}}$ and $\mathrm{Nu_{avg}}^{\mathrm{hb}}$. It has also been noted that the $\mathrm{Nu_{avg}}^{\mathrm{hf}}$ and

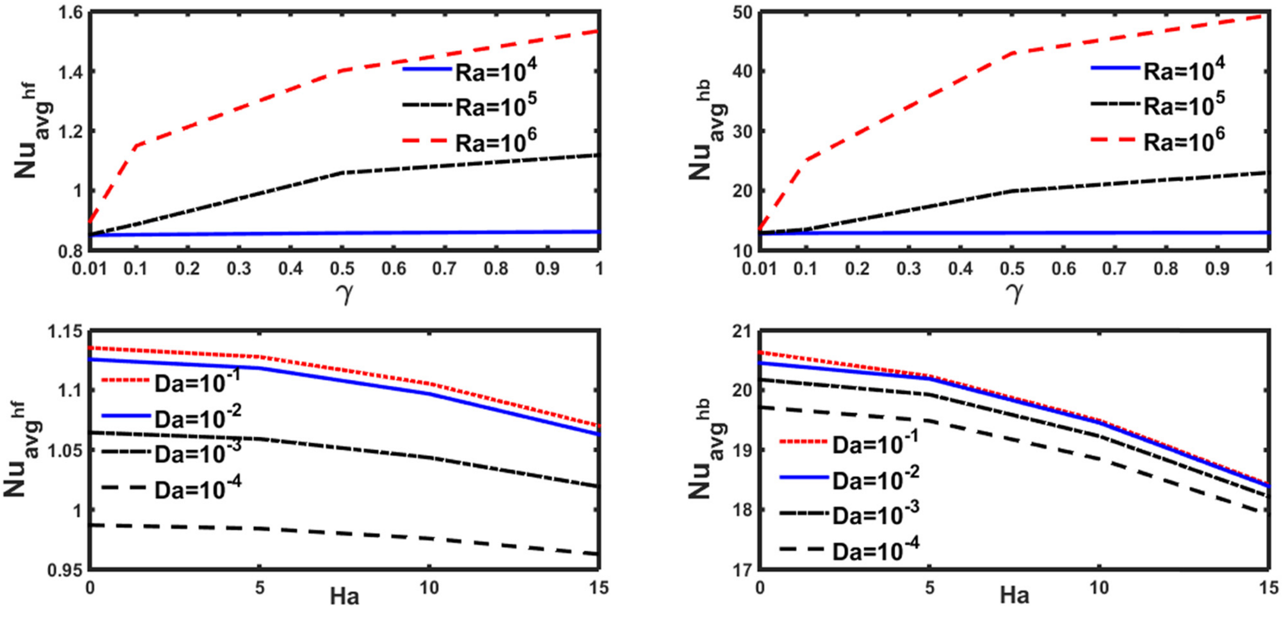

Figure 15: Effect of Ra and Da on $\mathrm{Nu_{avg}}^{\mathrm{hf}}$ and $\mathrm{Nu_{avg}}^{\mathrm{hb}}$ with variations in γ and Ha.

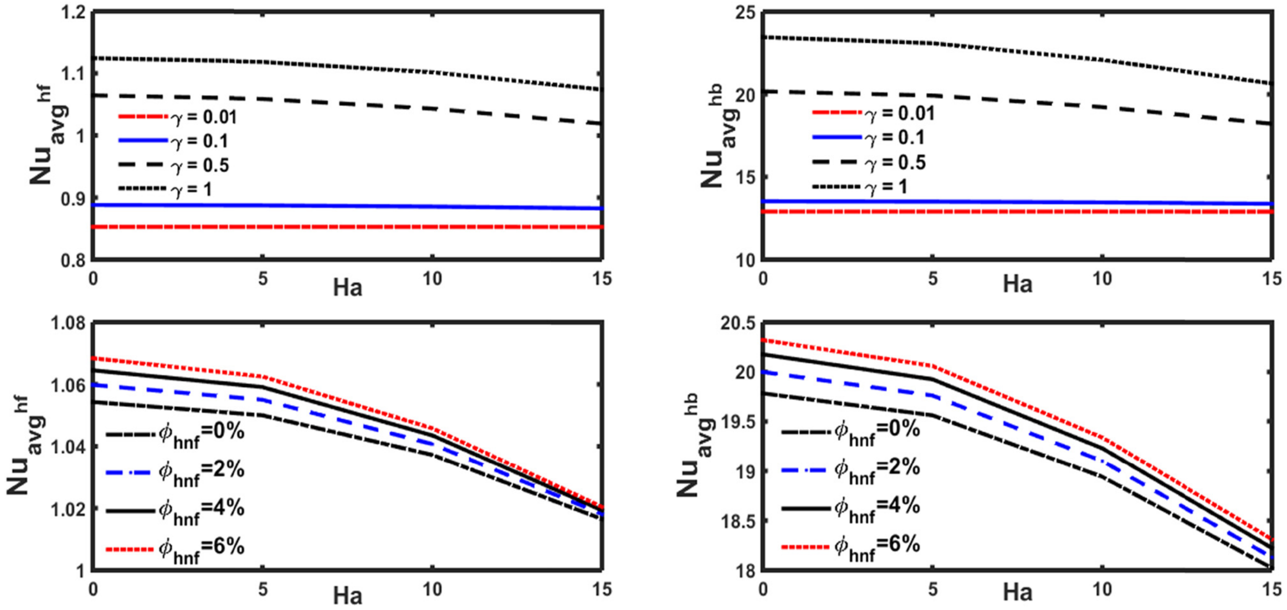

Figure 16: Influence of γ and ϕ_{hnf} on $\mathrm{Nu}_{\mathrm{avg}^{\mathrm{hf}}}$ and $\mathrm{Nu}_{\mathrm{avg}^{\mathrm{hb}}}$ with variation in Ha.

$\mathrm{Nu_{avg}}^{\mathrm{hb}}$ strongly increase with increasing Ra. As the magnitude of the magnetic field intensifies, the Lorentz forces experience a corresponding augmentation in their strength, and heat convection slows down for any value of Da, as shown in Figure 15. In addition, for any given value of Ha, both $\mathrm{Nu_{avg}}^{\mathrm{hf}}$ and $\mathrm{Nu_{avg}}^{\mathrm{hb}}$ decrease as the K decreases. At fixed Da = 10^{-3} and AR = 2/5, Table 3 shows that $\mathrm{Nu_{avg}}^{\mathrm{hf}}$ and $\mathrm{Nu_{avg}}^{\mathrm{hb}}$ decrease by 4.24 and 9.69%, respectively, as Ha increases from 0 to 15. Figure 16 exhibits the effect of γ and ϕ_{hnf} on $\mathrm{Nu_{avg}}^{\mathrm{hf}}$ and $\mathrm{Nu_{avg}}^{\mathrm{hb}}$ with variation in Ha. Both $\mathrm{Nu_{avg}}^{\mathrm{hf}}$ and $\mathrm{Nu_{avg}}^{\mathrm{hb}}$ increase as the Casson fluid parameter (γ) and ϕ_{hnf} rises. It has been found that the impact of Ha is negligible on $\mathrm{Nu_{avg}}^{\mathrm{hf}}$ and $\mathrm{Nu_{avg}}^{\mathrm{hb}}$ for small values of γ = 0.01, 0.1. As the γ and ϕ_{hnf} rise, both $\mathrm{Nu_{avg}}^{\mathrm{hf}}$ and $\mathrm{Nu_{avg}}^{\mathrm{hb}}$ increase for a fixed Ha; additionally, a reduction is observed with the rise in Ha.

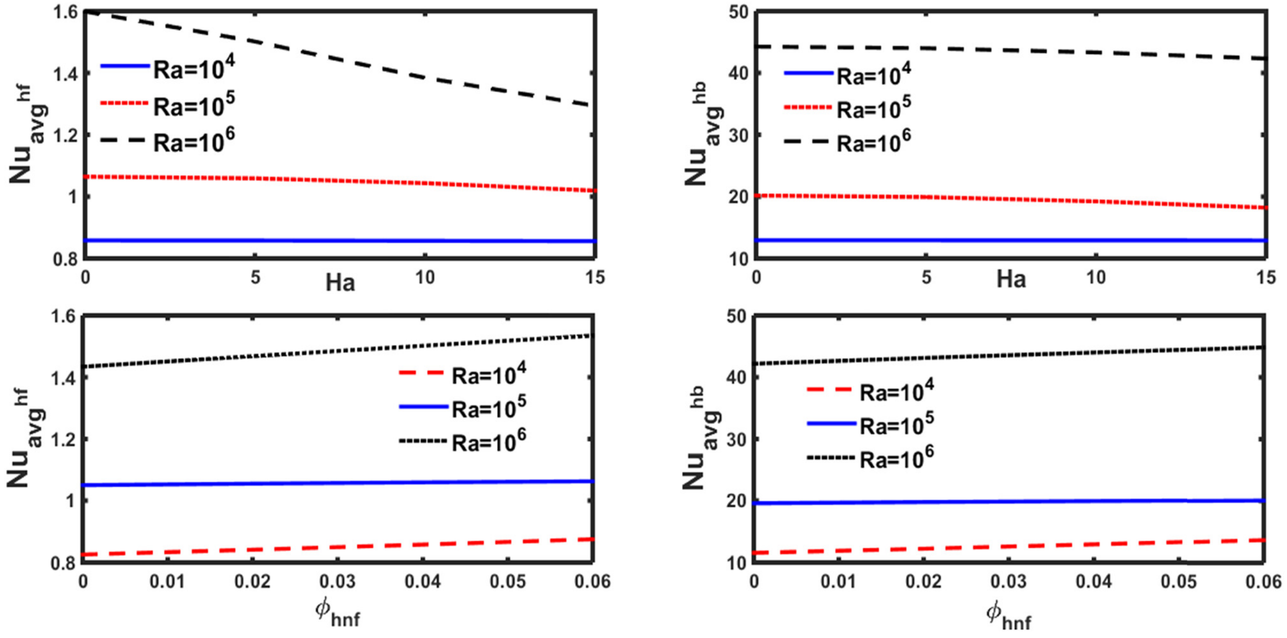

Figure 17: Influence of Ra on $\mathrm{Nu}_{\mathrm{avgl}^{\mathrm{hf}}}$ and $\mathrm{Nu}_{\mathrm{avg}^{\mathrm{hb}}}$ with variation in Ha and ϕ_{hnf}.

Also, Figure 16 shows that the attenuation in $\mathrm{Nu_{avg}}^{\mathrm{hf}}$ and $\mathrm{Nu_{avg}}^{\mathrm{hb}}$ is more noticeable with an increase in ϕ_{hnf} than with a rise in γ. In Figure 17, the effects of buoyancy force, measured in terms of Ra, on $\mathrm{Nu_{avg}}^{\mathrm{hf}}$ and $\mathrm{Nu_{avg}}^{\mathrm{hb}}$, *versus* Ha and ϕ_{hnf} are expressed. As the buoyancy force rises, a substantial rise in $\mathrm{Nu_{avg}}^{\mathrm{hf}}$ and $\mathrm{Nu_{avg}}^{\mathrm{hb}}$ is noticed for the fixed value of Ha and ϕ_{hnf}. The incorporation of nanoparticles enhances the thermal conductivity of hybrid nanofluids; consequently, an improvement in the process of heat transfer has been observed. While an appreciable reduction is noticed in $\mathrm{Nu_{avg}}^{\mathrm{hf}}$ and $\mathrm{Nu_{avg}}^{\mathrm{hb}}$ with the rise in Ha, as shown in Figure 17. The results presented in Table 3 show that $\mathrm{Nu_{avg}}^{\mathrm{hf}}$ and $\mathrm{Nu_{avg}}^{\mathrm{hb}}$ are affected by the AR of the rectangular heated cavity. Results demonstrate that as the AR is reduced, both $\mathrm{Nu_{avg}}^{\mathrm{hf}}$ and $\mathrm{Nu_{avg}}^{\mathrm{hb}}$ boost up significantly. Comparatively, the increase in $\mathrm{Nu_{avg}}^{\mathrm{hb}}$ is more obvious than in $\mathrm{Nu_{avg}}^{\mathrm{hf}}$. Table 4 shows the results of an estimation of $\mathrm{Nu_{avg}}^{\mathrm{hf}}$ and $\mathrm{Nu_{avg}}^{\mathrm{hb}}$ utilizing two different fluids, *i.e.*, Micropolar and Casson, having the same type of hybrid nanoparticles at various concentrations. Particularly in comparison to micropolar fluid, $\mathrm{Nu_{avg}}^{\mathrm{hf}}$ reduces while $\mathrm{Nu_{avg}}^{\mathrm{hb}}$ improves, when Casson fluid is utilized to fill the enclosure. For both fluids, *i.e.*, Micropolar and Casson, $\mathrm{Nu_{avg}}^{\mathrm{hf}}$ and $\mathrm{Nu_{avg}}^{\mathrm{hb}}$ are found to decrease as the porous medium's porosity increases. Also, a reduction in $\mathrm{Nu_{avg}}^{\mathrm{hf}}$ and $\mathrm{Nu_{avg}}^{\mathrm{hb}}$ is observed as ϕ_{hnf} reduces. The findings in Table 4 indicate that hybrid nanoparticles are found to be superior to single nanoparticle in regard to their effectiveness. The results presented in Table 4 show that $\mathrm{Nu_{avg}}^{\mathrm{hf}}$ and $\mathrm{Nu_{avg}}^{\mathrm{hb}}$ are affected by the AR of the heated rectangular cavity. Results demonstrate that as the AR is reduced, both $\mathrm{Nu_{avg}}^{\mathrm{hf}}$ and $\mathrm{Nu_{avg}}^{\mathrm{hb}}$ boost significantly. Comparatively, the increase in $\mathrm{Nu_{avg}}^{\mathrm{hb}}$ is more obvious than in $\mathrm{Nu_{avg}}^{\mathrm{hf}}$.

The findings of this study have very important physical implications in the applications involving natural convection in enclosures with porous media and hybrid nanofluids. For example, the enhancement in heat transfer with the increase of Ra highlights the critical role of buoyancy-driven flow in the promotion of convective heat transfer, which is vital for optimizing cooling processes in electronic devices and solar thermal collectors. The impact of Da on the flow structure and thermal performances indicates that the selection of porous materials with appropriate permeability can lead to a significant influence on the effectiveness of thermal insulation systems and porous heat exchangers. The suppression of the fluid motion with Ha provides valuable insights for designing MHD systems where the control of the flow and thermal characteristics is required, such as in nuclear reactors and MHD generators. In addition, the results present a dependence of the heat transfer on γ and ϕ_{hnf} which is important for fluid rheology and thermal conductivity enhancements allowing the achievement of efficient energy management. Finally, the sensitivity of the heat transfer to the AR emphasizes the need for careful geometric optimization in applications such as energy storage devices and compact heat exchangers.

Table 4: Comparative study of $\mathrm{Nu_{avg}}^{\mathrm{hf}}$ and ($\mathrm{Nu_{avg}}^{\mathrm{hb}}$) when Ra = 10^5, Da = 10^{-5}, and a constant heat flux of length H/2, centrally positioned at the bottom wall of the enclosure and filled with Casson hybrid nanofluid (current study) and micropolar hybrid nanofluid (Ahlawat and Sharma [44])

ϕ_{cu}	$\phi_{\mathrm{Al_2O_3}}$	ϕ_{hnf}	ε	$\mathrm{Nu_{avg}}^{\mathrm{hf}}$ **(Casson fluid (current study)/ micropolar fluid [44]**	$\mathrm{Nu_{avg}}^{\mathrm{hb}}$ **(Casson fluid (current study)/ micropolar fluid [44]**
0.00	0.00	0.00	0.398	1.0959/1.2107	09.9708/09.6153
0.05	0.05	0.10	0.260	1.2268/1.3481	13.8803/11.3845
0.05	0.05	0.10	0.398	1.2200/1.3406	13.8866/11.3727
0.05	0.05	0.10	0.476	1.2161/1.3364	13.8890/11.3678
0.025	0.025	0.05	0.398	1.1532/1.2746	11.8487/10.4722
0.02	0.03	0.05	0.398	1.1530/1.2742	11.8502/10.4586
0.03	0.02	0.05	0.398	1.1534/1.2749	11.8466/10.4853
0.04	0.06	0.10	0.398	1.2197/1.3396	13.8878/11.3457
0.06	0.04	0.10	0.398	1.2203/1.3414	13.8840/11.3989
0.10	0.00	0.10	0.398	1.1068/1.3447	13.3004/11.5003
0.00	0.10	0.10	0.398	1.1062/1.3326	13.5910/11.1852

5 Conclusions

This study corresponds to a numerical investigation of the impacts of sinusoidal heat flux and an embraced heated rectangular cavity on natural convection in a square enclosure partially filled with a porous medium and containing a Casson-hybrid nanofluid under the influence of a horizontal magnetic field. The findings revealed the interplay of key parameters such as Ra, Da, Ha, γ, and ϕ_{hnf} on the heat transfer and flow dynamics. The main results include the following:

- The increase of Ra leads to an intensification of the fluid circulation and an enhancement of the convective heat transfer, evidenced by higher average Nusselt number values and pronounced isotherm distortions.
- The rise of Ha suppressed the convection currents, reduced flow velocity, and dampened heat transfer due to the Lorentz force, which led to a stabilization of the flow.

- Higher Da causes better promotion of the fluid flow through the porous layer, which boosts the heat transfer, while lower Da restricts flow and traps heat near the source.
- The increase of γ causes a reduction of the fluid viscosity, facilitating stronger convection currents and better thermal performance.
- The enhancement of ϕ_{hnf} leads to an improved thermal conductivity of the hybrid nanofluid and results in a marked increase in heat transfer efficiency.
- Reducing the AR of the heated cavity significantly boosted heat transfer, with the influence being more pronounced in the porous region.

Limitations of the study:

The limitations of the research problem could include the following points:

1. The focus on a square enclosure and specific heating mechanisms limits the exploration of other geometries, heating patterns, and cavity shapes, which may be more relevant for certain engineering applications.
2. The absence of experimental data to validate the numerical findings may raise questions about the accuracy and reliability of the conclusions when applied to real-world systems.
3. The study may not address the environmental impact or cost-effectiveness of using hybrid nanofluids and porous materials in real-world applications, which are critical for sustainable development.

Addressing these limitations in future studies could enhance the reliability, applicability, and broader impact of the findings.

6 Future scope

This work unveils the effects of sinusoidal heat flux and heated rectangular cavity on natural convection within a square enclosure, partially filled with porous medium, offering novel insights into heat transfer dynamics. However, numerous possibilities remain open for further investigation to improve the understanding and application of this research problem:

1) Incorporating temperature-dependent thermal properties of the hybrid nanofluid enhances model accuracy, making it more reflective of real-world conditions.
2) Employing optimization techniques to identify the best configurations for sinusoidal heat flux amplitude, porous medium properties, and nanoparticle volume fractions would aid in designing efficient thermal systems.
3) Experimental validation of numerical results would enhance reliability and establish a benchmark for future theoretical research.
4) Enhancing heat transfer efficiency through diverse fluids and nanoparticles.

Acknowledgments: Anil Ahlawat would like to express gratitude to the Council for Scientific and Industrial Research (CSIR), New Delhi, India, for the financial support through letter no. 09/752(0073)-EMR-I. We extend our thanks to DST, New Delhi, for providing computational facilities under DST-FIST. Princess Nourah bint Abdulrahman University Researchers Supporting Project number (PNURSP2025R41), Princess Nourah bint Abdulrahman University, Riyadh, Saudi Arabia.

Funding information: Anil Ahlawat would like to express gratitude to the Council for Scientific and Industrial Research (CSIR), New Delhi, India, for the financial support through letter no. 09/752(0073)-EMR-I. Princess Nourah bint Abdulrahman University Researchers Supporting Project number (PNURSP2025R41), Princess Nourah bint Abdulrahman University, Riyadh, Saudi Arabia.

Author contributions: Anil Ahlawat: Methodology, Formal analysis, Software, Writing – original draft, Writing – review & editing. Mukesh Kumar Sharma: Methodology, Formal analysis, Conceptualization, Validation, Writing – review & editing. Kaouther Ghachem: Methodology, Formal analysis, Writing – review & editing. Badr M. AlShammari: Methodology, Formal analysis, Writing – review & editing. Lioua Kolsi: Methodology, Formal analysis, Writing – original draft, Writing – review & editing, Data curation. All authors have accepted responsibility for the entire content of this manuscript and approved its submission.

Conflict of interest: The authors state no conflict of interest.

References

[1] Choi SUS, Eastman JA. Enhancing thermal conductivity of fluids with nanoparticles. Argonne, IL (United States): Argonne National Lab. (ANL); 1995.

[2] Das SK, Choi SUS, Patel HE. Heat transfer in nanofluids – a review. Heat Transf Eng. 2006;27(10):3–19.

[3] Murshed SMS, Leong KC, Yang C. Investigations of thermal conductivity and viscosity of nanofluids. Int J Therm Sci. 2008;47(5):560–8.

[4] Sarkar J. A critical review on convective heat transfer correlations of nanofluids. Renew Sustain Energy Rev. 2011;15(6):3271–7.

[5] Yu W, Xie H. A review on nanofluids: preparation, stability mechanisms, and applications. J Nanomater. 2012;2012:1–17.

[6] Wu JM, Zhao J. A review of nanofluid heat transfer and critical heat flux enhancement – research gap to engineering application. Prog Nucl Energy. 2013;66:13–24.

[7] Tawfik MM. Experimental studies of nanofluid thermal conductivity enhancement and applications: A review. Renew Sustain Energy Rev. 2017;75:1239–53.

[8] Reddy KS, Kamnapure NR, Srivastava S. Nanofluid and nanocomposite applications in solar energy conversion systems for performance enhancement: a review. Int J Low-Carbon Technol. 2017;12(1):1–23.

[9] Jana S, Salehi-Khojin A, Zhong WH. Enhancement of fluid thermal conductivity by the addition of single and hybrid nano-additives. Thermochim Acta. 2007;462(1–2):45–55.

[10] Al Kalbani KS, Rahman MM, Alam S, Al-Salti N, ltayeb EA. Buoyancy induced heat transfer flow inside a tilted square enclosure filled with nanofluids in the presence of oriented magnetic field. Heat Transf Eng. 2018;39(6):511–25.

[11] Mansour MA, Siddiqa S, Gorla RSR, Rashad AM. Effects of heat source and sink on entropy generation and MHD natural convection of Al_2O_3-Cu/water hybrid nanofluid filled with square porous cavity. Therm Sci Eng Prog. 2018;6:57–71.

[12] Rashad AM, Armaghani T, Chamkha AJ, Mansour MA. Entropy generation and MHD natural convection of a nanofluid in an inclined square porous cavity: effects of a heat sink and source size and location. Chin J Phys. 2018;56(1):193–211.

[13] Armaghani T, Rashad AM, Vahidifar O, Mishra SR, Chamkha AJ. Effects of discrete heat source location on heat transfer and entropy generation of nanofluid in an open inclined L-shaped cavity. Int J Numer Methods Heat Fluid Flow. 2019;29(4):1363–77.

[14] Ushachew EG, Sharma MK, Rashidi MM. Heat transfer enhancement with nanofluid in an open enclosure due to discrete heaters mounted on sidewalls and a heated inner block. Int J Numer Methods Heat Fluid Flow. 2021;31(7):2172–96.

[15] Nishad S, Jain S, Bhargava R. Numerical simulation of natural convection within wavy square enclosure filled with nanofluid under magnetic field using EFGM with parallel algorithm. Int J Numer Methods Heat Fluid Flow. 2021;31(12):3505–26.

[16] Sun Q, Pop I. Free convection in a triangle cavity filled with a porous medium saturated with nanofluids with flush mounted heater on the wall. Int J Therm Sci. 2011;50(11):2141–53.

[17] Chamkha AJ, Ismael MA. Conjugate heat transfer in a porous cavity filled with nanofluids and heated by a triangular thick wall. Int J Therm Sci. 2013;67:135–51.

[18] Sheremet MA, Oztop HF, Pop I, Abu-Hamdeh N. Analysis of entropy generation in natural convection of nanofluid inside a square cavity having hot solid block: Tiwari and Das' model. Entropy. 2016;18(1):1–15.

[19] Sharma MK, Manjeet C, Makinde OD. Flow and heat transfer in nanofluid flow through a cylinder filled with foam porous medium under radial injection. Defect Diffus Forum. 2018;387:166–81.

[20] Vedavathi N, Venkatadri K, Fazuruddin S, Raju GSS. Natural convection flow in semi-trapezoidal porous enclosure filled with alumina-water nanofluid using Tiwari and Das' nanofluid model. Eng Trans. 2022;70(4):303–18.

[21] Venkatadri K, Fazuruddin S, Anwar Bég O, Ramesh O. Natural convection of nanofluid flow in a porous medium in a right-angle trapezoidal enclosure: a Tiwari and Das' nanofluid model. J Taibah Univ Sci. 2023;17(1):2263224.

[22] Venkatadri K, Saravana R, Bég OA, Kuharat S, Leonard HJ. Robust finite difference scheme for the magnetohydrodynamics natural convection in a quadrant-shaped enclosure with radiation effect. Eur Phys J Plus. 2024;139(8):702.

[23] Casson N. A flow equation for pigment-oil suspensions of the printing ink type. Rheology of disperse systems. New York: Pergamon; 1959. p. 84–104.

[24] Pop I, Sheremet M. Free convection in a square cavity filled with a Casson fluid under the effects of thermal radiation and viscous dissipation. Int J Numer Methods Heat Fluid Flow. 2017;27(10):2318–32.

[25] Hamid M, Usman M, Khan ZH, Haq RU, Wang W. Heat transfer and flow analysis of Casson fluid enclosed in a partially heated trapezoidal cavity. Int Commun Heat Mass Transf. 2019;108:104284.

[26] Aghighi MS, Metivier C, Masoumi H. Natural convection of Casson fluid in a square enclosure. Multidiscip Model Mater Struct. 2020;16(5):1245–59.

[27] Aneja M, Chandra A, Sharma S. Natural convection in a partially heated porous cavity to Casson fluid. Int Commun Heat Mass Transf. 2020;114:104555.

[28] Devi TS, Lakshmi CV, Venkatadri K, Prasad VR, Bég OA, Reddy MS. Simulation of unsteady natural convection flow of a Casson viscoplastic fluid in a square enclosure utilizing a MAC algorithm. Heat Transf. 2020;49(4):1769–87.

[29] Sivasankaran S, Bhuvaneswari M, Alzahrani AK. Numerical simulation on convection of non-Newtonian fluid in a porous enclosure with non-uniform heating and thermal radiation. AEJ – Alex Eng J. 2020;59(5):3315–23.

[30] Yasmin A, Ali K, Ashraf M. MHD Casson nanofluid flow in a square enclosure with non-uniform heating using the Brinkman model. Eur Phys J Plus. 2021;136(2):1–14.

[31] Munir S, Turabi YUUB. Impact of heated wavy wall and hybrid nanofluid on natural convection in a triangular enclosure with embedded cold cylinder under inclined magnetic field. Arab J Sci Eng. 2025;50(6):4007–20.

[32] Hussain S, Shoeibi S, Armaghani T. Impact of magnetic field and entropy generation of Casson fluid on double diffusive natural convection in staggered cavity. Int Commun Heat Mass Transf. 2021;127:105520.

[33] Ganesh NV, Al-Mdallal QM, Öztop HF, Kalaivanan R. Analysis of natural convection for a Casson-based multiwall carbon nanotube nanofluid in a partially heated wavy enclosure with a circular obstacle in the presence of thermal radiation. J Adv Res. 2022;39:167–85.

[34] Turabi YUUB, Munir S. CFD simulations of MHD effects on mixed convectional flow in a lid-driven square cavity with square cylinder using Casson fluid. Numer Heat Transf, Part B: Fundam. 2024;1–16. doi: 10.1080/10407790.2024.2365890.

[35] Suresh S, Venkitaraj KP, Selvakumar P, Chandrasekar M. Synthesis of Al_2O_3–Cu/water hybrid nanofluids using two step method and

its thermos-physical properties. Colloids Surf A: Physicochem Eng Asp. 2011;388:41–8.

[36] Suresh S, Venkitaraj KP, Selvakumar P, Chandrasekar M. Effect of Al_2O_3–Cu/water hybrid nanofluid in heat transfer. Exp Therm Fluid Sci. 2012;38:54–60.

[37] Ghalambaz M, Doostani A, Izadpanahi E, Chamkha AJ. Conjugate natural convection flow of Ag–MgO/water hybrid nanofluid in a square cavity. J Therm Anal Calorim. 2020;139(3):2321–36.

[38] Maxwell JA. A treatise on electricity and magnetism, Vol. 1, Oxford, UK: Clarendon Press; 1873.

[39] Brinkman HC. The viscosity of concentrated suspensions and solutions. J Chem Phys. 1952;20(4):571–81.

[40] Chamkha AJ, Ismael MA. Natural convection in differentially heated partially porous layered cavities filled with a Nanofluid. Numer Heat Transf; A: Appl. 2014;65(11):1089–113.

[41] Chamkha AJ, Ismael MA. Conjugate heat transfer in a porous cavity heated by a triangular thick wall. Numer Heat Transf; A: Appl. 2013;63(2):144–58.

[42] Jani S, Mahmoodi M, Amini M. Magnetohydrodynamic free convection in a square cavity heated from below and cooled from other walls. Int J Mech Indus Sci Eng. 2013;7(4):331–6.

[43] Malvandi A, Moshizi SA, Ganji DD. Effect of magnetic fields on heat convection inside a concentric annulus filled with Al_2O_3–water nanofluid. Adv Powder Technol. 2014;25(6):1817–24.

[44] Ahlawat A, Sharma MK. Effects of heated block comprised porous stratum and micropolar hybrid nanofluid on convective heat transfer and entropy generation in a square enclosure. Heat Transf. 2022;51(6):5320–47.